EUROPEAN ORGANIZATION FOR NUCLEAR RESEARCH

Production of light nuclei and anti-nuclei
in pp and Pb–Pb collisions at LHC energies

ALICE Collaboration[*]

Abstract

The production of (anti-)deuteron and (anti-)^{3}He nuclei in Pb–Pb collisions at $\sqrt{s_{NN}}$ = 2.76 TeV has been studied using the ALICE detector at the LHC. The spectra exhibit a significant hardening with increasing centrality. Combined blast-wave fits of several particles support the interpretation that this behavior is caused by an increase of radial flow. The integrated particle yields are discussed in the context of coalescence and thermal-statistical model expectations. The particle ratios, ^{3}He/d and ^{3}He/p, in Pb–Pb collisions are found to be in agreement with a common chemical freeze-out temperature of $T_{chem} \approx 156$ MeV. These ratios do not vary with centrality which is in agreement with the thermal-statistical model. In a coalescence approach, it excludes models in which nucleus production is proportional to the particle multiplicity and favors those in which it is proportional to the particle density instead. In addition, the observation of 31 anti-tritons in Pb–Pb collisions is reported. For comparison, the deuteron spectrum in pp collisions at $\sqrt{s}$ = 7 TeV is also presented. While the p/π ratio is similar in pp and Pb–Pb collisions, the d/p ratio in pp collisions is found to be lower by a factor of 2.2 than in Pb–Pb collisions.

[*]See Appendix A for the list of collaboration members

1   Introduction

Collisions of ultra-relativistic ions create suitable conditions for producing light (anti-)nuclei, because a high energy density is reached over a large volume. Under these conditions, hot and dense matter, which contains approximately equal numbers of quarks and anti-quarks at mid-rapidity, is produced for a short duration (a few 10^{-23} s). The system cools down and undergoes a transition to a hadron gas. While the hadronic yields are fixed at the moment when the rate of inelastic collisions becomes negligible (chemical freeze-out), the transverse momentum distributions continue to change until also elastic interactions cease (kinetic freeze-out).

The formation of (anti-)nuclei is very sensitive to the chemical freeze-out conditions, to the dynamics of the emitting source as well as to final-state effects. The production scenarios are typically discussed within two approaches: (i) The thermal-statistical approach has been very successful not only in describing the integrated yield of the hadrons but also of composite nuclei [1–3]. In this picture, the chemical freeze-out temperature T_{chem} (predicted around 160 MeV) acts as the key parameter. The strong sensitivity of the abundance of nuclei to the choice of T_{chem} is caused by their large mass m and the exponential dependence of the yield on the temperature given by $\exp(-m/T_{\text{chem}})$. (ii) In the coalescence model, nuclei are formed by protons and neutrons which are nearby in phase space and exhibit similar velocities [4, 5]. A quantitative description of this process is typically based on the coalescence parameter B_A and has been applied to many collision systems at various energies [6–13]. The binding energy of light nuclei is very small (around few MeV), so they can hardly remain intact during hadronic interactions, even if only quasi-elastic scattering during the hadronic phase with temperatures between 100 MeV and 170 MeV is considered. When produced thermally at chemical freeze-out, they might break apart and be created again by final-state coalescence [14]. It turns out that both, the thermal approach and the coalescence mechanism, give very similar predictions [15].

The production of light nuclei has attracted attention already at lower incident energies in heavy-ion collisions at the AGS, SPS, and RHIC [16–18]. A study of the dependence on $\sqrt{s_{\text{NN}}}$ is of particular interest, because different production mechanisms might dominate at various energies, e.g. a formation via spectator fragmentation at lower energies or via coalescence/thermal mechanisms at higher ones. In all cases, an exponential drop in the yield was found with increasing mass of the nuclei [19, 20]. At RHIC and now at the LHC, matter with a high content of strange and of anti-quarks is created in heavy-ion collisions. This has led to the first observation of anti-alphas [21] and of anti-hypertritons [22]. Their yields at LHC energies were predicted based on thermal model estimates in [1, 2].

In this paper, a detailed study of light (anti-)nuclei produced in the mid-rapidity region in Pb–Pb collisions at $\sqrt{s_{\text{NN}}} = 2.76$ TeV and a comparison with deuteron production in pp collisions at $\sqrt{s} = 7$ TeV using A Large Ion Collider Experiment (ALICE) [23] is presented. The paper is organized as follows: In Section 2, details of the analysis technique used to extract raw yields, acceptance and efficiency corrections of (anti-)deuterons and (anti-)^{3}He are presented. The results are given in Section 3 which starts with a comparison of the production of nuclei and anti-nuclei along with studies related to the hadronic interaction of anti-nuclei with the detector material. Then, the transverse momentum spectra, p_{T}-integrated yields and average transverse momenta are shown. The observation of (anti-)tritons is also discussed in this section. In Section 4, the results are discussed along with a description using a blast-wave approach, and are compared with expectations from the thermal-statistical and coalescence models. The measurement of (anti-)alphas and (anti-)hypertritons will be shown in subsequent publications.

2 Experiment and data analysis

2.1 The ALICE detector

The results presented in this paper are obtained from the data collected by the ALICE experiment at the LHC. Its performance and the description of its various subsystems are discussed in detail in Refs. [23, 24]. The ALICE detector has excellent particle identification capabilities. The main detectors used in this analysis are the Time Projection Chamber (TPC) [25], the Time-Of-Flight detector (TOF) [26], and the Inner Tracking System (ITS) [27]. All detectors are positioned in a solenoidal magnetic field of $B = 0.5$ T. As the main tracking device, the TPC provides full azimuthal acceptance for tracks in the pseudo-rapidity region $|\eta| < 0.8$. In addition, it provides particle identification via the measurement of the specific energy loss dE/dx. It allows the identification of (anti-)^{3}He over the entire momentum range under study and the measurement is only limited by the available statistics. The velocity information from the TOF detector is in addition used to identify deuterons with transverse momenta (p_T) above 1.4 GeV/c and (anti-)tritons in the transverse momentum range of 0.6 GeV/$c < p_T < 1.6$ GeV/c. The detector provides a similar acceptance as the TPC and its total time resolution for tracks from Pb–Pb collisions corresponds to about 80 ps which is determined by the intrinsic time resolution of the detector and the accuracy of the start time measurement. By a combined analysis of TPC and TOF data, deuterons are identified up to 4.5 GeV/c in Pb–Pb collisions. In case of pp collisions, the less precisely determined start time leads to a time resolution of about 120 ps and the identification is limited to about 3 GeV/c. The precise space-point resolution in the six silicon layers of the ITS allows a precise separation of primary and secondary particles in the high track density region close to the primary vertex.

2.2 Event and track selection

For this analysis, the data collected in the year 2010 are used. In total, the data sample consists of nearly 14 million Pb–Pb collisions at $\sqrt{s_{NN}} = 2.76$ TeV and 380 million minimum-bias triggered events for pp collisions at $\sqrt{s} = 7$ TeV after off-line event selection.

A pair of forward scintillator hodoscopes, the V0 detectors ($2.8 < \eta < 5.1$ and $-3.7 < \eta < -1.7$), measured the arrival time of particles with a resolution of 1 ns and was used for triggering purposes and for centrality determination of Pb–Pb collisions. In pp collisions, the data were collected using a minimum-bias trigger requiring at least one hit in either of the V0 detectors or in the two innermost layers of the ITS (Silicon Pixel Detector, SPD). The trigger condition during the Pb–Pb data taking was changed with time to cope with the increasing luminosity delivered by the LHC. It was restricted offline to a homogenous condition, requiring at least two hits in the SPD and one hit in either of the V0 detectors. This condition was shown to be fully efficient for the 90% most central events [28]. A signal in the V0 was required to lie in a narrow time window (≈ 30 ns) around the nominal collision time in order to reject any contamination from beam-induced background. Only events with a reconstructed primary vertex position in the fiducial region $|V_z| < 10$ cm were considered in the analysis. The V0 amplitude distribution was also used to determine the centrality of the heavy-ion collisions. It was fitted with a Glauber Monte-Carlo model to compute the fraction of the hadronic cross section corresponding to a given range of V0 amplitude. Based on those studies, the data were divided in several centrality percentiles, selecting on signal amplitudes measured in the V0 [28]. The contamination from electromagnetic processes has been found to be negligible for the 80% most central events.

In this analysis, the production of primary deuterons and ^{3}He-nuclei as well as their respective anti-particles are measured at mid-rapidity. In order to provide optimal particle identification by reducing the difference between transverse and total momentum, the spectra are provided within a rapidity window of $|y| < 0.5$. In addition, only those tracks in the full tracking acceptance of $|\eta| < 0.8$ are selected. The extrapolation of the yield at low momenta, where the acceptance does not cover the full $|y| < 0.5$ region, is done by assuming a flat distribution in y and by determining $d\eta/dy$ for each p_T-interval. Primary
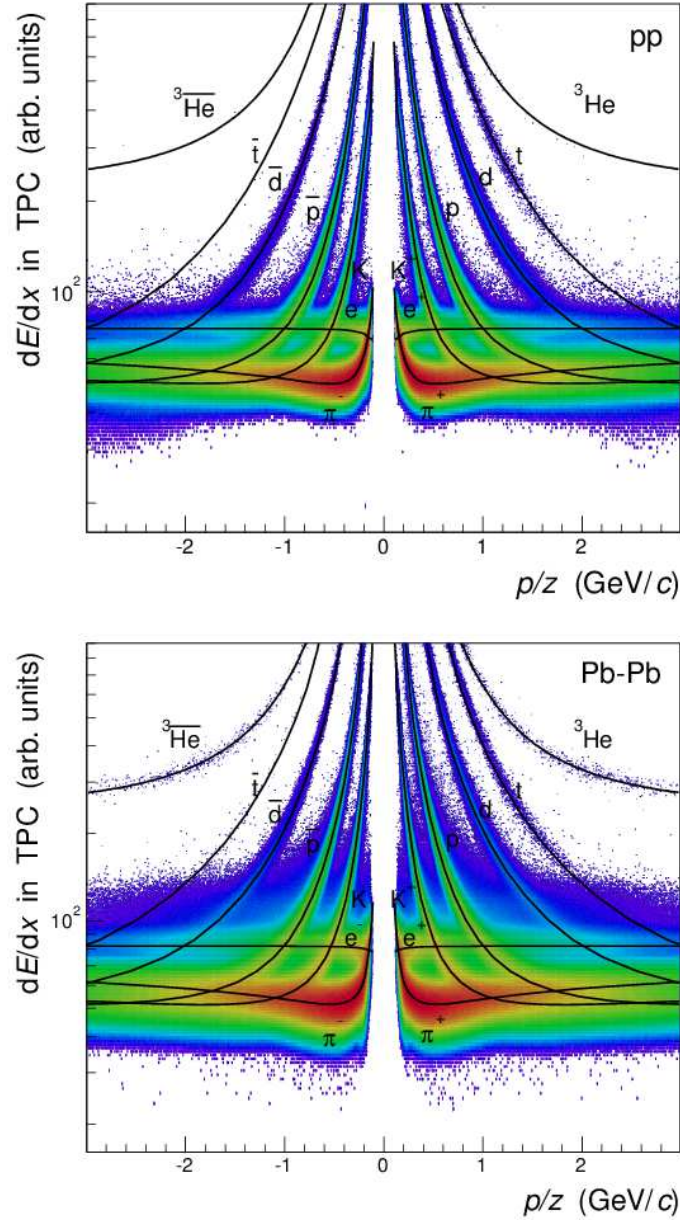
Fig. 1: Specific energy loss (dE/dx) vs. rigidity (momentum/charge) for TPC tracks from pp collisions at $\sqrt{s}$ = 7 TeV (top panel) and from 0-80% most central Pb–Pb collisions at $\sqrt{s_{NN}}$ = 2.76 TeV (bottom panel). The solid lines represent a parametrization of the Bethe-Bloch curve.

particles are defined as prompt particles produced in the collision including all decay products, except products from weak decays of light flavor hadrons and of muons. In order to select primary tracks of suitable quality, various track selection cuts are applied. At least 70 clusters in the TPC and two points in the ITS (out of which at least one in the SPD) are required. These selections guarantee a track momentum resolution of 2% in the relevant p_T-range and a dE/dx resolution of about 6%, as well as a determination of the Distance-of-Closest-Approach to the primary vertex in the plane perpendicular (DCA$_{xy}$) and parallel (DCA$_z$) to the beam axis with a resolution of better than 300 μm in the transverse direction [24]. Furthermore, it is required that the χ^2 per TPC cluster is less than 4 and tracks of weak-decay products are rejected as they cannot originate from the tracks of primary nuclei.
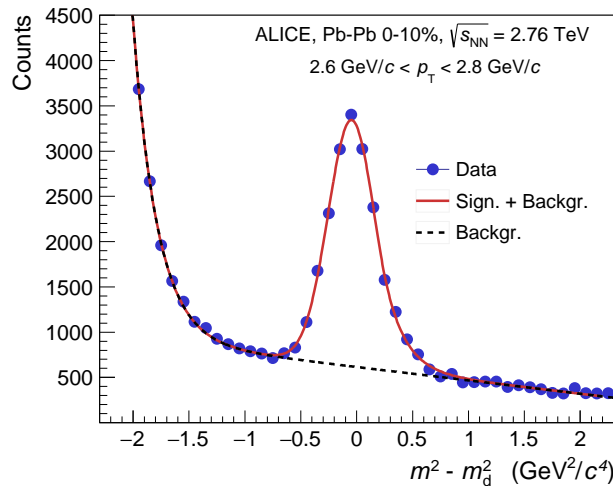
4

Fig. 2: Distribution of $(m^2 - m_d^2)$ measured with the TOF detector for tracks with $2.6\,\mathrm{GeV}/c < p_T < 2.8\,\mathrm{GeV}/c$ from central Pb–Pb collisions showing the peak corresponding to the deuteron mass m_d and the background from mismatched tracks (black dotted line) which is subtracted to obtain the raw yields (see text for details).

2.3 Particle identification

Particle identification is mainly performed using the TPC [25]. It is based on the measurement of the specific ionization energy deposit (dE/dx) of charged particles. Figure 1 shows the dE/dx versus rigidity (momentum/charge, p/z) of TPC tracks for pp collisions at $\sqrt{s} = 7$ TeV (top panel) and for Pb–Pb collisions at $\sqrt{s_{NN}} = 2.76$ TeV (bottom panel). Nuclei and anti-nuclei like (anti-)deuterons, (anti-)tritons, and (anti-)^{3}He are clearly identified over a wide range of momenta. The solid curves represent a parametrization of the Bethe-Bloch function for the different particle species. In practice, it is required that the measured energy-loss signal of a track lies in a 3σ window around the expected value for a given mass hypothesis. While this method provides a pure sample of ^{3}He nuclei in the p_T-range between 2 GeV/c and 7 GeV/c, it is limited to about $p_T < 1.4$ GeV/c for deuterons.

In order to extend the p_T-reach of the deuteron measurement, the TOF system is used above this momentum in addition. Based on the measured flight time t, the mass m of a particle can be calculated as

$$m^2 = \frac{p^2}{c^2} \cdot \left(\frac{c^2 t^2}{L^2} - 1 \right), \tag{1}$$

where the total momentum p and the track length L are determined with the tracking detectors. Figure 2 shows the obtained Δm^2 distribution, where the deuteron mass square (m_d^2) was subtracted, for a p_T-bin between 2.6 GeV/c and 2.8 GeV/c. For each p_T-bin, the Δm^2 distribution is fitted with a Gaussian function with an exponential tail for the signal. Since the background mainly originates from two components, namely wrong associations of a track with a TOF cluster and the non-Gaussian tail of lower mass particles, it is described with a first order polynomial to which an exponential function is added. The same procedure for signal extraction and background subtraction is applied in the analysis of pp collisions.

2.4 Background rejection

Particles produced in the collisions might interact with the detector material and the beam pipe which leads to the production of secondary particles. The probability of anti-nucleus production from the

5

interaction of primary particles with detector material is negligible, whereas the sample of nuclei may include primary as well as secondary particles originating from the material. This contamination is exponentially decreasing with increasing momentum. In addition, it is about five times larger in central compared to peripheral Pb–Pb or pp events because of the higher probability of a fake ITS hit assignment to secondary tracks. Most of the secondary particles from material have a large DCA to the primary vertex and hence this information is used to correct for the contamination. Figure 3 shows the DCA_{xy} distribution for deuterons (left panel) and anti-deuterons (right panel) for Pb–Pb collisions at $\sqrt{s_{\mathrm{NN}}} =$ 2.76 TeV. The distributions are shown for two different $|\mathrm{DCA}_z|$ cuts. As can be seen from the figure, a strict $|\mathrm{DCA}_z|$ cut of 1.0 cm cuts a large fraction of background for nuclei, but does not change the distribution for anti-nuclei. At sufficiently high momenta (above 1.4 GeV/c for deuterons and above 2 GeV/c for ^{3}He), the secondary and knock-out contamination caused by material is in this way reduced to a negligible level and the raw yield can be directly extracted. In order to extend the measurement of deuterons to lower momenta in Pb–Pb collisions, the DCA_{xy} distribution for deuterons in each transverse momentum (p_{T})-interval was fitted with the expected shapes (called "templates" in the following) as extracted from Monte-Carlo events. Figure 4 shows a typical example of this procedure for tracks with transverse momentum range 0.9 GeV/$c < p_{\mathrm{T}} <$ 1.0 GeV/c. One template for primary particles and one template for secondary particles from material are used. The characteristic shape of the template used for knock-out nuclei from material with its flat behavior at large DCA_{xy} allows a precise distinction between the two contributions. The significant peak at small $|\mathrm{DCA}_{xy}|$ is caused by those knock-out nuclei to which a cluster in one of the SPD layers is wrongly associated. The obtained fraction of primary particles is then used to calculate the raw yield in the corresponding p_{T}-bin. The same technique is applied for background rejection and raw yield extraction of deuterons for pp collisions at $\sqrt{s} =$ 7 TeV.

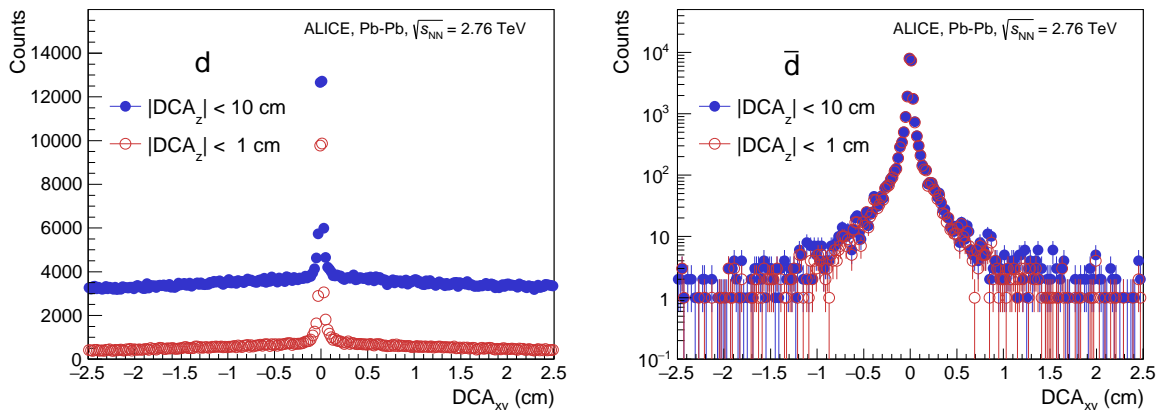**Fig. 3:** Distribution of DCA_{xy} for deuterons (left) and anti-deuterons (right) in the transverse momentum range 0.7 GeV/$c < p_{\mathrm{T}} <$ 1.4 GeV/c for 0–80% most central Pb–Pb collisions at $\sqrt{s_{\mathrm{NN}}} =$ 2.76 TeV demonstrating the influence of cuts in DCA_z on d and $\overline{\mathrm{d}}$.

2.5 Efficiency and acceptance

The final p_{T}-spectra of nuclei are obtained by correcting the raw spectra for tracking efficiency and acceptance based on Monte-Carlo (MC) generated events. Standard event generators, such as PYTHIA [29], PHOJET [30], or HIJING [31] do not include the production of (anti-)nuclei other than (anti-)protons and (anti-)neutrons. Therefore, nuclei are explicitly injected into underlying PYTHIA (in case of pp) and HIJING (in case of Pb–Pb) events with a flat momentum distribution. In the next step, the particles are propagated through the ALICE detector geometry with the GEANT3 transport code [32]. GEANT3 includes a basic description of the interaction of nuclei with the detector, however, this description is imperfect due to the limited data available on collisions of light nuclei with heavier materials. Due to the
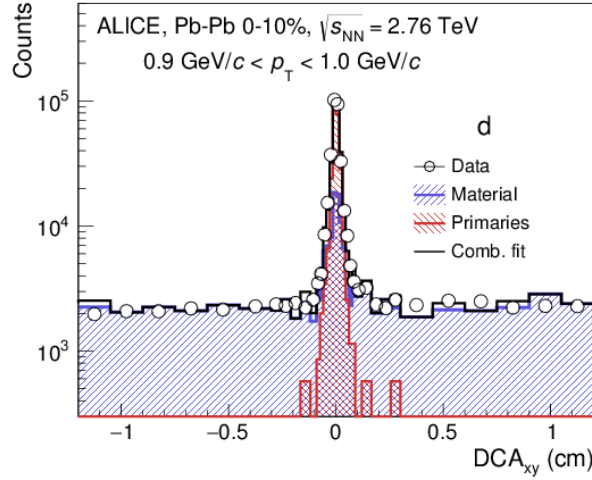
Fig. 4: Distribution of DCA_{xy} of identified deuterons in the transverse momentum range 0.9 GeV/c < p_T < 1.0 GeV/c for central Pb–Pb collisions ($\sqrt{s_{NN}}$ = 2.76 TeV) along with the Monte-Carlo templates which are fitted to the data (see text for details).

unknown interaction of anti-nuclei with material, these processes are not included for anti-nuclei heavier than anti-protons. In order to account for these effects, a full detector simulation with GEANT4 as a transport code [33, 34] was used. Following the approach described in [35], the correction for interaction of (anti-)nuclei with the detector material from GEANT3 was scaled to match the expected values from GEANT4. An alternative implementation to correct for this effect and the relevant uncertainties related to these corrections are discussed in Section 3.1. The acceptance×efficiency is then obtained as the ratio of the number of particles detected by the detector to the number of generated particles within the relevant phase space.
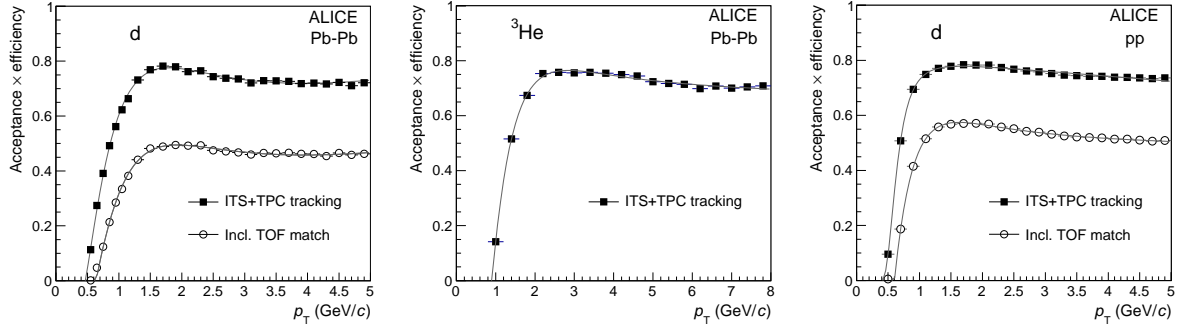

Fig. 5: Acceptance×efficiency as a function of transverse momentum (p_T) for deuterons (left) and for ^{3}He (middle) in Pb–Pb collisions at $\sqrt{s_{NN}}$ = 2.76 TeV, as well as for deuterons in pp collisions at $\sqrt{s}$ = 7 TeV (right panel). The curves represent a fit with the function presented in Eq. (2) (see text for details).

The top panel of Fig. 5 shows the acceptance×efficiency for deuterons (left) and ^{3}He (right) as a function of p_T for Pb–Pb collisions at $\sqrt{s_{NN}}$ = 2.76 TeV. In both cases, the rapid rise of the efficiency at low p_T is determined by energy loss and multiple scattering processes of the incident particle with the detector material. The values reach a maximum when the energy loss becomes smaller and when the track curvature is still sufficiently large so that a track can cross the dead area between two TPC readout chambers in a relatively small distance such that the two track parts can still be connected. For straighter tracks at higher p_T which cross the insensitive region between two chambers this distance is larger and the con-

nection becomes more difficult. Thus a slight reduction of the efficiency is observed until a saturation value is reached. The figure also shows the lower efficiency values (open points) when in addition a deuteron track is matched to a hit in the TOF detector. The drop is mainly caused by the energy loss and multiple scattering in the material between the TPC and the TOF, by the TOF dead zones corresponding to other detectors or structures, and by the number of active TOF channels. The curves represent fits with the empirical functional form

$$f(p_{\mathrm{T}}) = a_0 \; e^{(-a_1/p_{\mathrm{T}})^{a_2}} + a_3 \; p_{\mathrm{T}} \; . \tag{2}$$

Here, a_0, a_1, a_2, and a_3 are free parameters. Correcting the raw spectra with either the fit function or the actual histogram is found to result in negligible differences with respect to the total systematic error.

Figure 5 (bottom panel) also shows acceptance×efficiency for the deuterons as a function of p_{T} for pp collisions at $\sqrt{s} = 7$ TeV. The curve is a fit using the same functional form as used for the Pb–Pb collisions discussed above. The efficiency has a similar p_{T}-dependence as the one for Pb–Pb collisions at $\sqrt{s_{\mathrm{NN}}}$ = 2.76 TeV. The observed differences are due to variations in the number of active detector components, mainly in the SPD, for the two data sets.
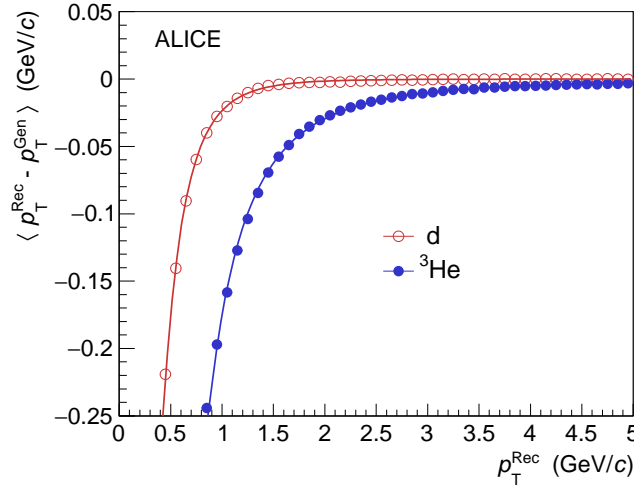
2.6 Momentum correction

Fig. 6: The average difference between the reconstructed and the generated p_{T} is plotted as a function of the reconstructed p_{T} for simulated deuterons and ^{3}He for Pb–Pb collisions at $\sqrt{s_{\mathrm{NN}}}$ = 2.76 TeV. The lines represent a fit with the functional form as shown in Eq. (3) (see text for details).

Low-momentum particles lose a considerable amount of energy while traversing the detector material. The track reconstruction algorithm takes into account the Coulomb scattering and energy loss, assuming the pion mass for each particle. Therefore, a track-by-track correction for the energy loss of heavier particles (d/d̄ and ^{3}He/$^3\overline{\mathrm{He}}$) is needed. This correction is obtained from MC simulations, in which the difference of the reconstructed and the generated transverse momentum is studied on a track-by-track basis. Figure 6 shows the average p_{T}-difference as a function of the reconstructed track momentum ($p_{\mathrm{T}}^{\mathrm{Rec}}$) for deuterons and ^{3}He. The lines represent the empirical function

$$f(p_{\mathrm{T}}) = A + B \left(1 + \frac{C}{p_{\mathrm{T}}^2} \right)^D , \tag{3}$$

where the free parameters A, B, C, and D are extracted from a fit. It can be seen that the correction becomes largest for the heaviest particles at low momenta. This reflects the typical $1/\beta^2$-behavior of the energy loss. The difference in transverse momentum is corrected on a track-by-track basis in the analysis. This energy loss correction has been applied both for pp and for Pb–Pb collisions. The same correction in rapidity has also been studied and found to result in negligible changes in the final spectra.

2.7   Systematic uncertainties

Individual contributions to the systematic error of the measurement are summarized in Table 1 and are discussed in detail in the following. The systematic uncertainty related to the identification of the nuclei is smaller in the p_T-region in which the energy loss in the TPC provides a clear separation compared to those in which the identification is mainly based on the TOF information. The error is of the order of 1% for deuterons at low momenta and for the full p_T-range studied for ^{3}He-nuclei. In the TOF part ($p_T >$ 1.4 GeV/c) of the deuteron spectrum, the error is considerably larger due to the presence of background and has been estimated as 5% on the basis of different signal extraction methods: the raw yields obtained from the signal fit and from bin counting are compared. The estimates of the uncertainties related to the tracking and matching are based on a variation of the track cuts and are found to be less than 4% and independent of the particle species. In addition to this, a variation in the momentum correction leads to differences of similar magnitude at lower momenta and are added in quadrature.

Contamination from secondaries originating from interactions of primary particles with the detector material dominates the systematic error at low transverse momenta, but it decreases exponentially towards higher momenta. These uncertainties are estimated by a variation of the fit range and templates. Their values amount to about 20% in the lowest p_T-bin for deuterons and for ^{3}He in most central events. For all other centralities and transverse momentum regions, it is significantly lower. Feed down from weakly decaying hyper-nuclei is negligible for deuterons. The only relevant decay of the hyper-triton, $^3_\Lambda$H $\rightarrow$ d $+$ p $+$ π^-, results in a negligible contamination, because of the roughly 700 times smaller production cross section of the hyper-triton with respect to the deuteron [1, 2]. On the other hand, the decay $^3_\Lambda$H $\rightarrow$ ^{3}He $+$ π^- contaminates the ^{3}He-spectrum as these particles are produced with similar abundance. This background is conceptually similar to the feed down of Λ decays into the proton-spectrum [36] though the relevant branching ratio in the case of $^3_\Lambda$H (25%) [37] is assumed to be considerably lower than in the case of Λ (64%). A detailed MC study shows that only about 4-8% of all $^3_\Lambda$H decaying into ^{3}He pass the track selection criteria of primary ^{3}He. Therefore, the remaining contamination has not been subtracted and the uncertainty related to it was further investigated by a variation of the DCA$_{xy}$-cut in data and a final error of about 5% is assigned. Uncertainties in the material budget have been studied by simulating events varying the amount of material by $\pm10\%$. This leads to variations in the efficiency of about 5% in the lowest p_T-bins. The hadronic interaction of nuclei with the detector material gives rise to an additional uncertainty of about 6% for deuteron and for ^{3}He. The material between TPC and TOF needs to be considered only for the deuteron spectrum above $p_T >$ 1.4 GeV/c and increases the uncertainty by additional 5%. The corresponding corrections for anti-nuclei are significantly larger and less precisely determined because of the missing knowledge of the relevant elastic and inelastic cross sections. Details of the systematics originating from differences between the available models are discussed in the next section.

In general, the individual contributions to the systematic error do not show a significant dependence on the event multiplicity. The only exception is given by the uncertainty of the correction for secondaries from material, which changes from about 20% in central to about 4% in peripheral Pb–Pb or pp collisions, respectively. All other contributions are found to be independent of event multiplicity.

Source	d		^{3}He	
	0.7 GeV/c	4 GeV/c	2 GeV/c	8 GeV/c
PID	1%	5%	1%	1%
Tracking and matching	6%	4%	6%	4%
Secondaries material	20%	1%	20%	1%
Secondaries weak decay	negl.		5%	
Material budget	5%	1%	3%	1%
Hadronic interaction	6%		6%	

Table 1: Summary of the main contributions to the systematic uncertainties. See text for details.
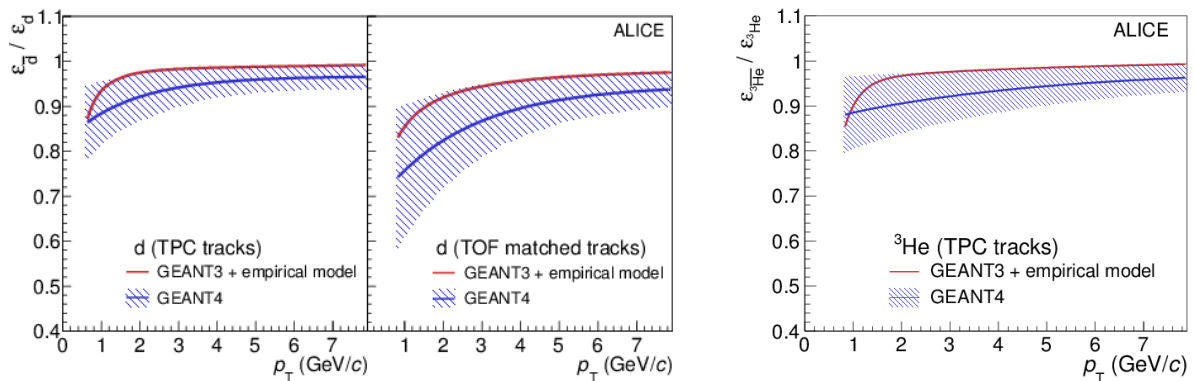

Fig. 7: Ratio of anti-particle to particle efficiency based on GEANT4 and a modified version of GEANT3 including an empirical model to describe the hadronic interaction of anti-nuclei for (anti-)deuterons (left) and for (anti-)^{3}He (right). The estimate of the systematic uncertainty for the hadronic interaction based on the difference between the two models is indicated by the blue band.

3   Results

3.1   Anti-particle to particle ratios and hadronic interaction of anti-nuclei

For a measurement of particle to anti-particle ratios, the correction of the hadronic interaction of the emitted particles with the detector material has to be precisely known. The relevant cross sections are only poorly measured for anti-nuclei heavier than $\bar{p}$. The only available data for anti-deuterons from the U-70 Serpukhov accelerator [38, 39] are measured at relatively high momenta ($p = 13.3$ GeV/c and $p = 25.0$ GeV/c) and provide only a rough constraint. Two approaches are considered to model the correction for hadronic interaction. Firstly, the anti-nuclei cross sections are approximated in a simplified empirical model by a combination of the anti-proton ($\sigma_{\bar{p},A}$) and anti-neutron ($\sigma_{\bar{n},A}$) cross sections. Following the approach presented in [40], the cross section $\sigma_{\bar{d},A}$ for an anti-deuteron on a target material with mass number A is then e.g. given by

$$\sigma_{\bar{d},A} = \left(\sigma_{\bar{p},A}^{3/2} + \sigma_{\bar{n},A}^{3/2}\right)^{2/3} K(A) , \qquad (4)$$

where the scaling factor $K(A)$ is determined from the same procedure applied to the measured inelastic cross sections of nuclei and protons. Details of the method can be found in [40]. This approach is implemented as a modification to GEANT3. However, it does not account for elastic scattering processes and is therefore only used for the estimation of the systematic uncertainty. Secondly, the anti-nucleus–nucleus cross sections are determined in a more sophisticated model with Glauber calculations based on the well-measured total and elastic p$\bar{p}$ cross section [34]. It is implemented in the GEANT4 software
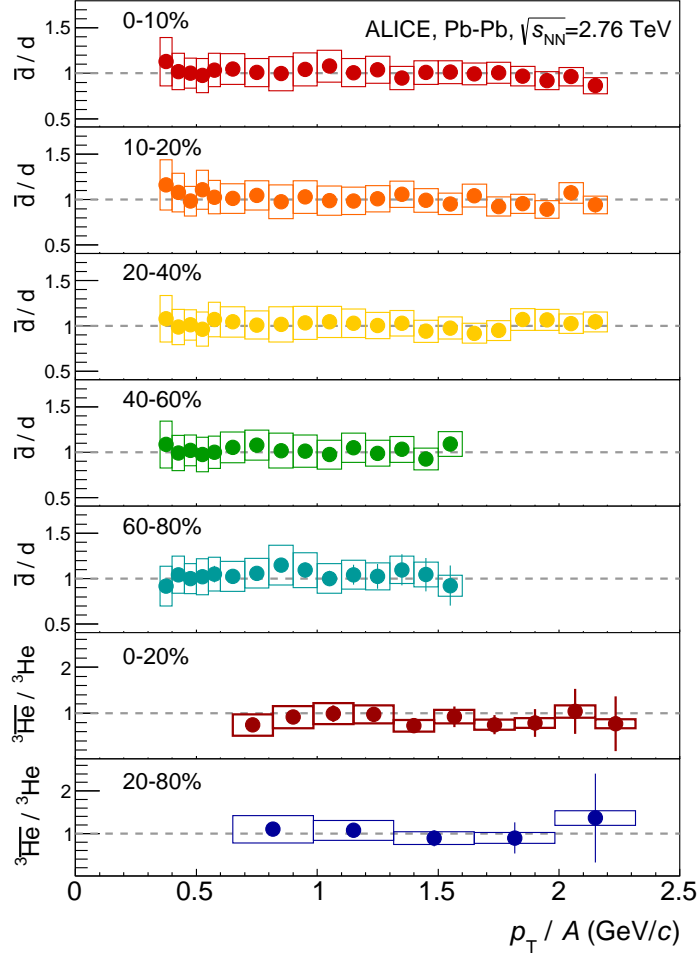
10

Fig. 8: Ratios of $\bar{\mathrm{d}}$ and d as well as of $^3\overline{\mathrm{He}}$ and $^3\mathrm{He}$ versus p_T per nucleon for various centrality classes in Pb–Pb collisions at $\sqrt{s_{NN}}$ = 2.76 TeV. Boxes describe the systematic uncertainties, vertical lines the statistical ones.

package [33].

The relevant correction factor for the anti-particle to particle ratio is given by the ratio of the efficiencies in which all effects cancel except of those related to the hadronic interaction with the detector material. The efficiency ratios for anti-deuterons and for $^3\overline{\mathrm{He}}$ nuclei using the two models described above (modified GEANT3 and GEANT4) are shown in Fig. 7. The applied correction factors are parameterized with the same function which was used for a similar study in [35]. The absorption correction is larger for tracks which are required to reach the TOF detector due to the additional material behind the TPC, mainly the support structure and the Transition Radiation Detector (TRD). In the following, results corrected with GEANT4 are presented. Based on the discrepancy between the two models, an uncertainty of 60% of the difference between the efficiency for particles and anti-particles is assumed for the absorption correction. It is indicated by the blue band in Fig. 7.

Applying this model-based correction to the data, leads to $\bar{\mathrm{d}}$/d and $^3\overline{\mathrm{He}}/^3\mathrm{He}$ ratio shown in Fig. 8 for various centrality bins in Pb–Pb collisions. Both ratios are consistent with unity and exhibit a constant behavior as a function of p_T as well as of collision centrality. Since the same statements hold true for the

Anti-nuclei/nuclei	Centrality	Ratio
$\bar{\mathrm{d}}$/d	0-10%	$0.98 \pm 0.01 \pm 0.13$
	10-20%	$0.99 \pm 0.01 \pm 0.13$
	20-40%	$1.01 \pm 0.01 \pm 0.14$
	40-60%	$1.02 \pm 0.01 \pm 0.16$
	60-80%	$1.02 \pm 0.02 \pm 0.16$
$^3\overline{\mathrm{He}}/^3\mathrm{He}$	0-20%	$0.83 \pm 0.08 \pm 0.16$
	20-80%	$1.03 \pm 0.14 \pm 0.18$

Table 2: Anti-particle to particle ratios for various centrality classes in Pb–Pb collisions at $\sqrt{s_{\mathrm{NN}}}$ = 2.76 TeV. The first error represents the statistical error and the second one is the systematic error. See text for details.

$\bar{\mathrm{p}}$/p ratios [41], these observations are in agreement with expectations from the thermal-statistical and coalescence models [2] which predict a ratio of $\bar{\mathrm{d}}/\mathrm{d} = (\bar{\mathrm{p}}/\mathrm{p})^2$ and $^3\overline{\mathrm{He}}/^3\mathrm{He} = (\bar{\mathrm{p}}/\mathrm{p})^3$. Table 2 show the anti-particle to particle ratios for various centrality classes in Pb–Pb collisions at $\sqrt{s_{\mathrm{NN}}}$ = 2.76 TeV.

Ongoing studies on the hadronic interaction of anti-nuclei in the material between the TPC and TOF will allow to constrain the uncertainties of the currently purely model based corrections and to replace them with data driven ones. As the spectra for nuclei and anti-nuclei are consistent within the currently large uncertainties, only the spectra of nuclei are provided in the following.

3.2   Spectra of nuclei

The final spectra of deuterons obtained in Pb–Pb and pp collisions are shown in Fig. 9. The statistical and systematic errors are shown separately as vertical lines and boxes, respectively. In pp collisions, the spectrum is normalized to the number of all inelastic collisions (N_{INEL}) which includes a correction for trigger inefficiencies (see [42, 43] for details). It is fitted with the following function [44–46] that has been used for lighter particles

$$\frac{1}{2\pi p_{\mathrm{T}}}\frac{\mathrm{d}^2 N}{\mathrm{d}p_{\mathrm{T}}\mathrm{d}y} = \frac{\mathrm{d}N}{\mathrm{d}y}\frac{(n-1)(n-2)}{2\pi\, nC(nC + m_0(n-2))}\left(1 + \frac{m_{\mathrm{T}} - m_0}{nC}\right)^{-n} \qquad (5)$$

with the fit parameters C, n, and the dN/dy. The parameter m_0 corresponds to the mass of the particle under study (deuteron) at rest and $m_{\mathrm{T}} = \sqrt{m_0^2 + p_{\mathrm{T}}^2}$ to the transverse mass. As in the case of lighter particles, the function is found to describe the deuteron p_{T} spectrum well in the measured range with a χ^2/ndf of 0.26 . The fit function is used for the extrapolation to the unmeasured region at low and high transverse momenta (about 45% of the total yield) and a p_{T}-integrated yield of dN/dy = $(2.03 \pm 0.34(\mathrm{syst})) \times 10^{-4}$ is obtained.

While statistical errors are negligible, the systematic error is dominated by the uncertainty related to the extrapolation (13%) which is evaluated by a comparison of different fit functions [47] (Boltzmann, m_{T}-exponential, p_{T}-exponential, Fermi-Dirac, Bose-Einstein). Based on the same extrapolation in the unmeasured region of the spectrum, a mean transverse momentum $\langle p_{\mathrm{T}}\rangle$ of 1.075 ± 0.060 GeV/c is obtained.

The final spectra of deuterons and ^{3}He for Pb–Pb collisions at $\sqrt{s_{\mathrm{NN}}}$ = 2.76 TeV are shown in Figs. 9 and 10 for various choices of the collision centrality. Again, the systematic and statistical errors are shown separately by boxes and vertical lines, respectively. The p_{T} distributions show a clear evolution, becoming harder as the multiplicity increases. A similar behavior is observed for protons, which have been successfully described by models that incorporate a significant radial flow [41].

The spectra obtained in Pb–Pb collisions are individually fitted with the blast-wave (BW) model for the determination of p_{T}-integrated yields and $\langle p_{\mathrm{T}}\rangle$. This model [48] describes particle production properties
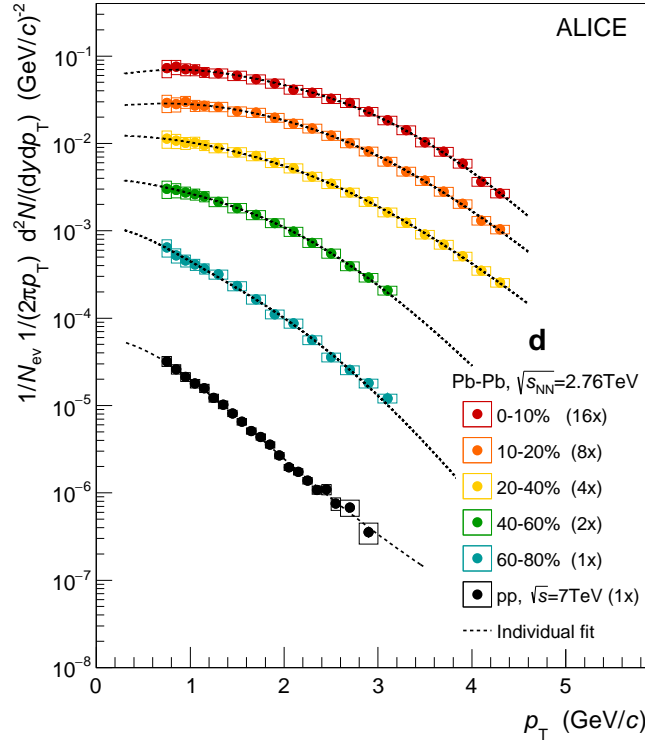
Fig. 9: Efficiency and acceptance corrected deuteron spectra for Pb–Pb collisions at $\sqrt{s_{NN}} = 2.76$ TeV in various centrality classes and for inelastic pp collisions at $\sqrt{s} = 7$ TeV. The dashed lines represent an individual fit with the BW function (Eq. 6) in the case of Pb–Pb spectra and with the function presented in Eq. (5) in the case of the pp spectrum (see text for details). The boxes show systematic error and vertical lines show statistical error separately.

by assuming that the particles are emitted thermally from an expanding source. The functional form of the model is given by

$$\frac{1}{p_T}\frac{dN}{dp_T} \propto \int_0^R r\,dr\,m_T I_0\left(\frac{p_T\sinh\rho}{T_{kin}}\right) K_1\left(\frac{m_T\cosh\rho}{T_{kin}}\right),\tag{6}$$

where the velocity profile ρ is described by

$$\rho = \tanh^{-1}\beta = \tanh^{-1}\left(\beta_S(r/R)^n\right).\tag{7}$$

Here I_0 and K_1 are the modified Bessel functions, r is the radial distance from the center of the fireball in the transverse plane, R is the radius of the fireball, $\beta(r)$ is the transverse expansion velocity, β_S is the transverse expansion velocity at the surface, n is the exponent of the velocity profile, and T_{kin} is the kinetic freeze-out temperature. The free parameters in the fit are T_{kin}, β_S, n, and a normalization parameter. Here, we present two alternatives: fitting the two particles separately (Figs. 9 and 10) and simultaneously (Fig. 11). The extracted values of the kinetic freeze-out temperature and radial flow velocity are discussed in more detail in the next section. The results of these fits are summarized in Table 3, where the values of dN/dy and $\langle p_T\rangle$ are also reported. The dN/dy values are extracted by individually fitting the spectra with the BW model. The extrapolation to $p_T = 0$ introduces an additional error which is again evaluated by a comparison of different fit functions and amounts to about 6% for central and 13% for peripheral collisions for the deuteron yields. In the ^{3}He case, it contributes about 17% and 16% to the total systematic errors for the 0–20% and 20-80% centrality class, respectively.
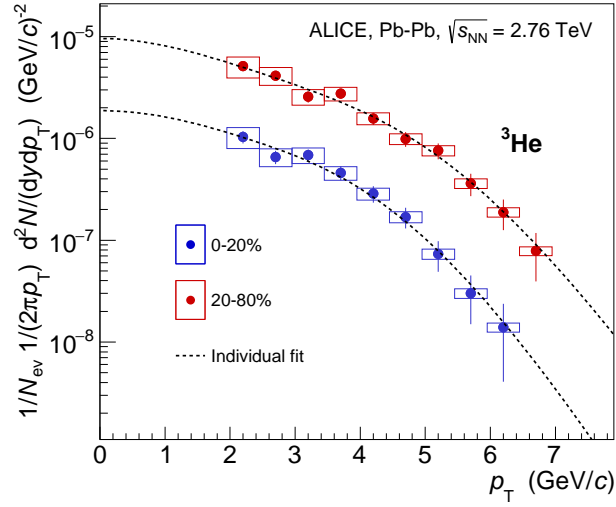
13

Fig. 10: ^{3}He spectra for two centrality classes (0–20% and 20–80%) are shown for Pb–Pb collisions at $\sqrt{s_{NN}} =$ 2.76 TeV. The spectra are fitted individually with the BW function (dashed lines). The systematic and statistical errors are shown by boxes and vertical lines, respectively.
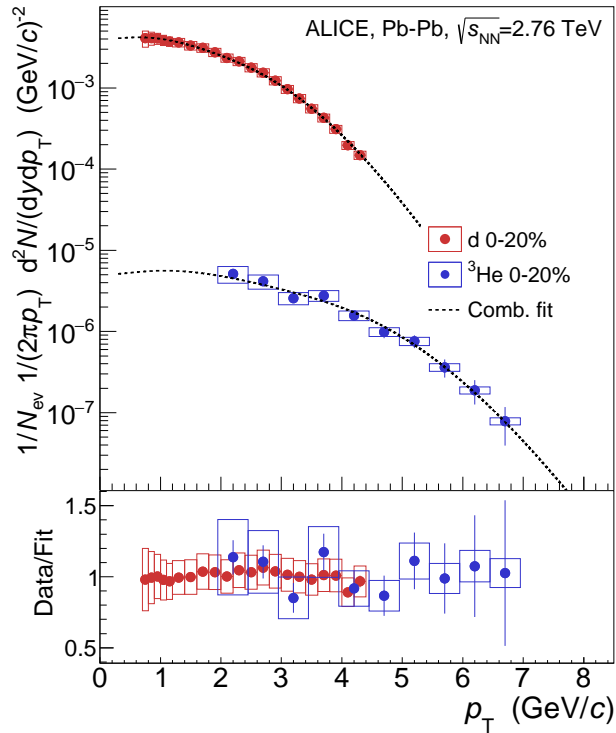

Fig. 11: The top panel shows the combined fit of deuteron and ^{3}He spectra with the BW function for 0–20% centrality for Pb–Pb collisions at $\sqrt{s_{NN}} =$ 2.76 TeV. The systematic and statistical errors are shown by boxes and vertical line, respectively. The lower panel shows the deviation of the spectra from the BW fits.

Centrality	$\langle \beta \rangle$	T_{kin} (MeV)	n	dN/dy	$\langle p_{\text{T}} \rangle$ (GeV/c)	χ^2/ndf
d (0-10%)	0.629 ± 0.003	77 ± 1	0.75 ± 0.05	$(9.82 \pm 0.04 \pm 1.46) \times 10^{-2}$	$2.12 \pm 0.00 \pm 0.09$	0.10
d (10-20%)	0.612 ± 0.004	106 ± 2	0.76 ± 0.06	$(7.60 \pm 0.04 \pm 1.16) \times 10^{-2}$	$2.08 \pm 0.01 \pm 0.09$	0.07
d (20-40%)	0.568 ± 0.005	124 ± 9	0.91 ± 0.12	$(4.75 \pm 0.02 \pm 0.77) \times 10^{-2}$	$1.92 \pm 0.00 \pm 0.11$	0.03
d (40-60%)	0.508 ± 0.012	109 ± 3	1.07 ± 0.16	$(1.90 \pm 0.01 \pm 0.40) \times 10^{-2}$	$1.64 \pm 0.01 \pm 0.10$	0.02
d (60-80%)	0.382 ± 0.009	109 ± 2	1.80 ± 0.31	$(0.51 \pm 0.01 \pm 0.14) \times 10^{-2}$	$1.29 \pm 0.01 \pm 0.14$	0.27
^{3}He (0-20%)	0.572 ± 0.006	101 ± 61	1.02 ± 0.02	$(2.76 \pm 0.09 \pm 0.62) \times 10^{-4}$	$2.83 \pm 0.05 \pm 0.45$	0.49
^{3}He (20-80%)	0.557 ± 0.007	101 ± 37	0.99 ± 0.03	$(5.09 \pm 0.24 \pm 1.36) \times 10^{-5}$	$2.65 \pm 0.06 \pm 0.45$	0.20
d, ^{3}He (0-20%)	0.617 ± 0.009	83 ± 22	0.81 ± 0.06			0.32

Table 3: Summary of extracted yields dN/dy and mean transverse momenta $\langle p_{\text{T}} \rangle$ based on the BW individual fits performed on the spectra for Pb–Pb collisions at $\sqrt{s_{\text{NN}}} = 2.76$ TeV. The first error on dN/dy and $\langle p_{\text{T}} \rangle$ represents the statistical error and the second one is the combination of systematic and extrapolation errors, added in quadrature. See text for details.
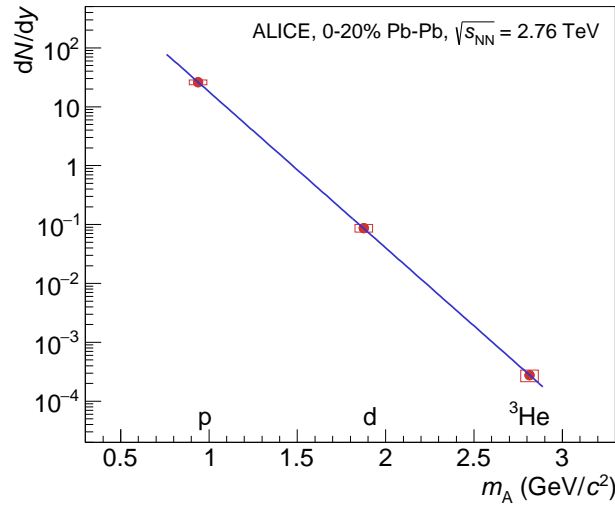

Fig. 12: The production yield dN/dy of light nuclei as a function of the particle mass m_{A} measured for 0-20% centrality class in Pb–Pb collisions at $\sqrt{s_{\text{NN}}} = 2.76$ TeV. The line represents a fit with an exponential function.

Figure 12 shows the production yields of p, d, and ^{3}He measured in the centrality interval 0–20% in Pb–Pb collisions which follow an exponential decrease with the mass of the particle. The penalty factor, namely the reduction of the yield by adding one nucleon, is 307 ± 76. Such an exponential decrease has already been observed at lower incident energies starting from those provided by the AGS [16, 18, 19, 21], yet with different slopes.

The mean transverse momentum $\langle p_{\text{T}} \rangle$ values obtained for d and ^{3}He are compared to those of light particle species for Pb–Pb collisions at $\sqrt{s_{\text{NN}}} = 2.76$ TeV (from [41]) in Fig. 13. The figure shows that the $\langle p_{\text{T}} \rangle$ increases with increasing mass of the particle. Such a behavior is expected if all the particles are emitted from a radially expanding source.

3.3 Observation of (anti-)triton

The combined particle identification capability of the TPC and TOF also allows a track-by-track identification of low momenta (0.6 GeV/c < p_{T} < 1.6 GeV/c) anti-tritons as illustrated in Fig. 14. In this momentum region, the background from mismatched tracks is removed by the TPC particle identification. The contamination is estimated based on a side-band study and found to be negligible below p_{T} < 1.6 GeV/c, but it increases rapidly for higher momenta so that signal and background cannot be
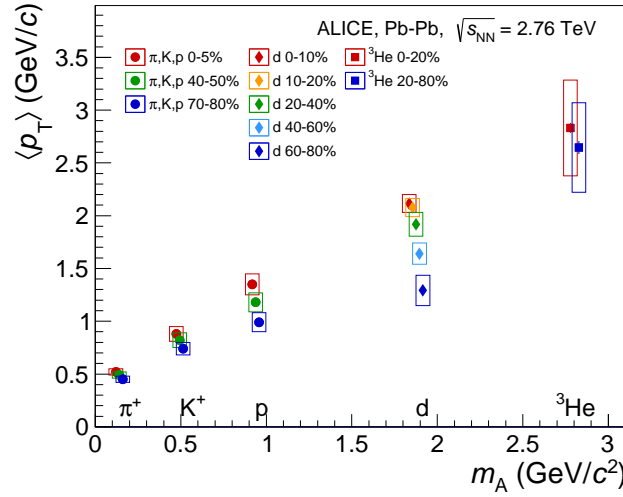
Fig. 13: Mean transverse momentum $\langle p_T \rangle$ as a function of particle mass for various centrality classes are shown for Pb–Pb collisions at $\sqrt{s_{NN}} = 2.76$ TeV.
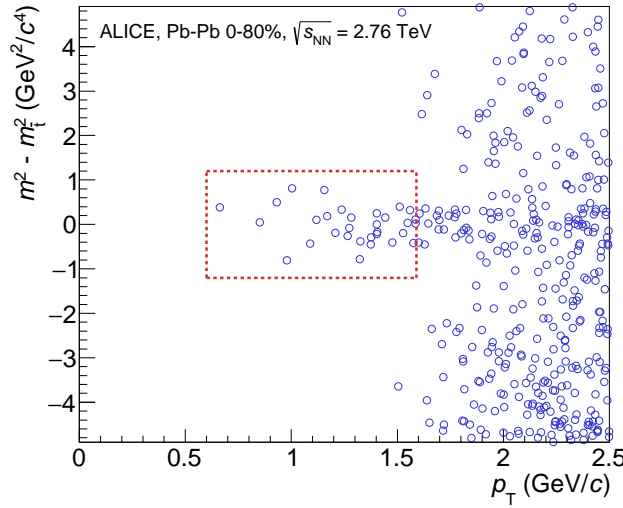

Fig. 14: Scatter plot of $(m^2 - m_{\bar{t}}^2)$ measured with the TOF detector versus p_T. Only those tracks are shown which pass the pre-selection done by applying a 3σ cut on the TPC dE/dx. The p_T-region in which the candidates are identified on a track-by-track basis is shown as red box.

distinguished anymore thus limiting the range available for the measurement.

As can be seen, 31 anti-triton candidates are observed in the 0-80% centrality range. These numbers are consistent with expectations based on an extrapolation of the ^{3}He-spectra to lower momenta taking into account the low reconstruction efficiency for anti-tritons in this momentum region (of about 11% $\pm$ 6%). An observation of about 10 to 40 anti-tritons is expected based on this estimate, indicating similar production rates of anti-tritons and $^3\overline{\text{He}}$ nuclei. This comparison suffers from large uncertainties related to the absorption of anti-nuclei and energy loss in the detector material before the TPC at such low momenta. A similar measurement of tritons is unfeasible due to the large contamination from knock-out nuclei in this momentum region.

4   Discussion
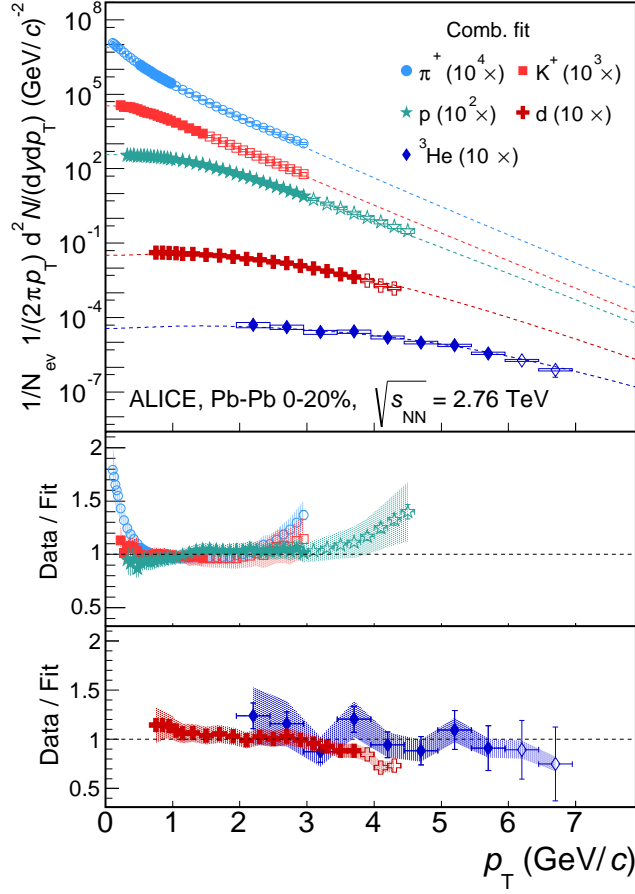
4.1   Description of spectra via blast-wave fits

Fig. 15: Blast-wave fit of π^+, K^+, p, d, and ^{3}He particles for 0–20% centrality for Pb–Pb collisions at $\sqrt{s_{NN}} = 2.76$ TeV. Solid symbols denote the p_T range of the spectra used for the fits, while the open symbols show the remaining part. The lower panels show the deviations of the measured spectra to the BW fits.

Combined BW fits provide essential insight into the kinetic freeze-out conditions and allow quantitative comparisons between different collision systems and between measurements at different $\sqrt{s_{NN}}$ in terms of a hydrodynamic interpretation. In this section, a simultaneous fit to the π, K, p, d, and ^{3}He spectra in the centrality range 0-20% using in addition data from [41, 49] is discussed. Since the BW model is not expected to describe eventual hard contributions that may set in at higher p_T, the fit ranges have been limited. For the light particles, they are taken as in [41, 49] (0.5-1 GeV/c, 0.2-1.5 GeV/c, 0.3-3 GeV/c for π, K, and p, respectively). However, for d and ^{3}He, the spectrum is fitted up to the p_T value where the invariant yield reduces to 10% of the maximum available value of that spectrum. The exponent n of the velocity profile is left as a free parameter as in [41]. In such an approach, all particle species are forced to decouple with the same parameters even though they feature different hadronic cross sections with the medium. This is in particular relevant for multi-strange particles such as Ξ and Ω [50], which are therefore not included in the fit. These limitations are not present in full hydrodynamic calculations. However, these are not yet available for light nuclei at LHC energies.

In Fig. 15 the results of a simultaneous fit to the five particle species are shown. The deviations of the

spectra from the BW fit are shown in the lower parts of Fig. 15. The statistical errors are shown by vertical lines and the systematic errors are shown as shaded bands. Note that data points marked with open symbols are not included in the fit. The hardening of the spectra for central collisions is qualitatively well described by the combined BW fit with a collective radial flow velocity $\langle \beta \rangle = 0.632 \pm 0.01$, a kinetic freeze-out temperature of $T_{kin} = 113 \pm 12$ MeV, and $n = 0.72 \pm 0.03$. The χ^2/ndf value of the fit is 0.4. A comparison of these parameters to those obtained from a fit to π, K, and p [41] ($\langle \beta \rangle = 0.644 \pm 0.020$, $T_{kin} = 97 \pm 15$ MeV, and $n = 0.73 \pm 0.11$) reveals that the inclusion of nuclei leads to a slightly smaller value for $\langle \beta \rangle$ and a slightly larger value for T_{kin}. This behavior is mainly driven by the strong anti-correlation of $\langle \beta \rangle$ and T_{kin} in the blast-wave model: the slightly lower value of $\langle \beta \rangle$ leads to a deviation of the fit from the proton spectrum which is then compensated by a higher T_{kin}.

A detailed look at the data-to-fit ratio for light nuclei reveals a considerable slope, both for d and ^{3}He, which is not observed in the case of a fit to light nuclei alone as shown in Fig. 11. The difference between the two fit variants is caused by a small, but significant change in $\langle \beta \rangle$ which is about 5% lower in the fit to light nuclei alone. This deviation thus underlines the strong sensitivity of the light nuclei spectra to the value of $\langle \beta \rangle$ due to their large mass.

4.2   Comparison to thermal models

Figure 16 shows the d/p and the ^{3}He/p ratios as a function of the average charged particle multiplicity per event. The proton yields are taken from [41, 49]. The observed values of about 3.6×10^{-3} for the d/p ratio and about 9.3×10^{-6} for the ^{3}He/p ratio are in agreement with expectations from the thermal-statistical models [1, 2]. Similar values for d/p ratios are also observed by the PHENIX experiment for Au-Au collisions [47, 51]. Since at RHIC energies significant differences between nucleus and anti-nucleus production are present, for this plot the geometrical mean is used which in a thermal concept cancels the influence of the baryon chemical potential (μ_B) *. Within the achieved experimental precision, no dependence of these particle ratios on the event multiplicity is observed at RHIC and LHC energies. Also the $\overline{p}$/p and the p/π ratios hardly vary with centrality [41, 52] showing that T_{chem} and μ_B do not vary with centrality in high energy collisions. In a coalescence approach, the centrality independence disfavors implementations in which the nuclei production is proportional to the absolute proton multiplicity [53] rather than the particle density.

The comparison with thermal models is shown in more detail in Fig. 17 for the 0–10% centrality class. These calculations have been performed using the grand-canonical formulation of both THERMUS [54] and the GSI-Heidelberg model [1]. This approach is appropriate for the ratios shown here, as no strange quarks are involved. Details can be found in [1, 2]. These ratios are monotonically increasing with T_{chem} reflecting the dependence with $\exp(-\Delta m/T_{chem})$ where Δm corresponds to the mass difference of the particles under study.

The measured ratios of ^{3}He/p and ^{3}He/d are in agreement with a chemical freeze-out temperature in the range of 150 MeV to 165 MeV. No significant differences are observed between the THERMUS and GSI-Heidelberg model with respect to the production of light (anti-)nuclei. A fit to p, d, and ^{3}He only gives $T_{chem} = 156 \pm 4$ MeV with a χ^2/ndf of 0.4. This value can be compared to a fit including all measured light flavor hadrons which yields a temperature of about 156 MeV [55].

The d/p ratio obtained in pp collisions is lower by a factor of 2.2 than in Pb–Pb collisions. Assuming thermal production not only in Pb–Pb, but also in pp collisions, this could indicate a lower freeze-out temperature in pp collisions. However, the p/π ratio does not show significant differences between pp and Pb–Pb collisions. Effects related to canonical suppression of strange particles can also be excluded

---

*In a thermal model, the yield n_B of a baryon with energy E in a medium of temperature T is proportional to $\exp(-\frac{E-\mu_B}{T})$ while the yield of an anti-baryon $n_{\overline{B}}$ is proportional $\exp(-\frac{E+\mu_B}{T})$. The geometric mean $\sqrt{n_B n_{\overline{B}}}$ leads to a cancellation of the μ_B.

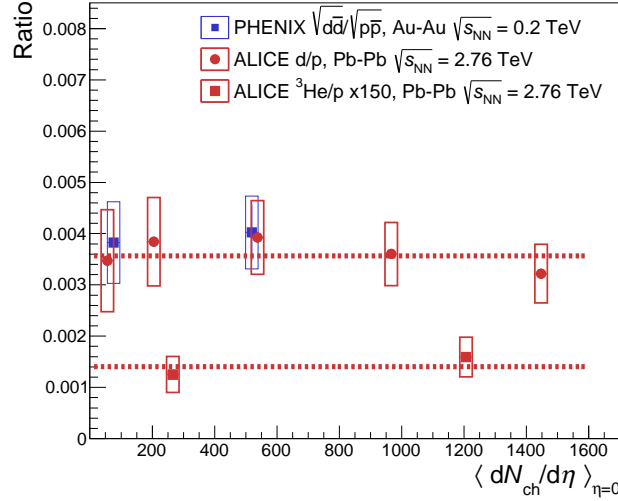**Fig. 16:** d/p and ^{3}He/p ratio in heavy-ion collisions as a function of event multiplicity. Within the uncertainties no significant variation with multiplicity is observed. The d/p and $\overline{d}/\overline{p}$ results from the PHENIX Collaboration [47, 51] are averaged as explained in the text. The lines represent fits with a constant to the ALICE data points.
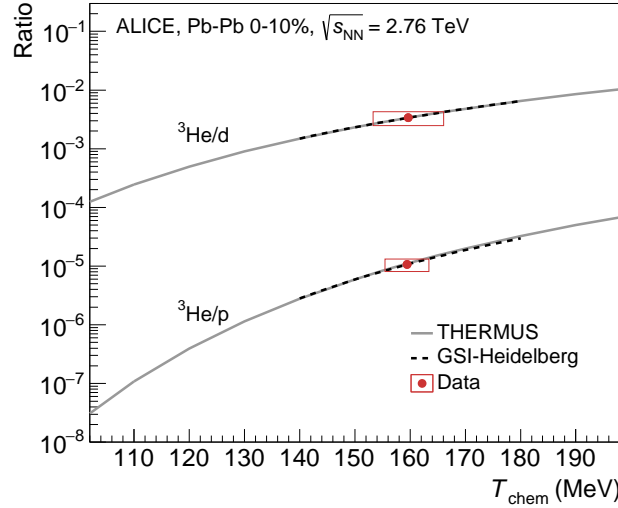

Fig. 17: Particle ratios of nuclei as measured in 0–10% most central Pb–Pb collisions compared to the THERMUS [54] model (solid lines) and the GSI-Heidelberg model [1] (dashed lines) as a function of the chemical freeze-out temperature T_{chem}. The ^{3}He yield is scaled to 0–10%. Horizontal error bars indicate the temperature range obtained by a projection of the total error of the ratio on the temperature axis.

because these ratios do not involve any strange quarks. Therefore, this observation must find another explanation within the framework of thermal models or non-thermal production mechanisms need to be considered in small systems. Further work in the theoretical models is needed for a better understanding of this effect.

4.3 Comparison with the coalescence model

Light nuclei have nucleons as constituents and are thus likely formed via coalescence of protons and neutrons which are near in space and have similar velocities. In this production mechanism, the spectral distribution of the composite nuclei is related to the one of the primordial nucleons via

$$E_i \frac{d^3 N_i}{dp_i^3} = B_A \left(E_p \frac{d^3 N_p}{dp_p^3} \right)^A \tag{8}$$

assuming that protons and neutrons have the same momentum distribution. B_A is the coalescence parameter for nuclei i with mass number A and a momentum of $p_i = A \, p_p$. In the simplest approach, B_A is independent of the transverse momentum and is determined by the maximum relative momentum p_0 of the coalescing nucleons [17, 56, 57]:

$$B_A = \left(\frac{4\pi}{3} p_0^3 \right)^{A-1} \frac{M}{m^A} . \tag{9}$$

In this expression, the spin of the nucleons is neglected and M and m are the nucleus and the proton mass, respectively. Under the assumption that the p_0 value is the same for deuterons and ^{3}He, Eq. (9) can be rewritten as

$$B_3 = B_2^2 \left(\frac{M_{^3\mathrm{He}} \cdot m}{M_d^2} \right) \approx \frac{3}{4} B_2^2 , \tag{10}$$

allowing for a basic comparison of the measured B_2 and B_3 values.

Figure 18 shows the obtained B_2 values for deuterons (left panel) and B_3 values for ^{3}He (right panel) in several centrality bins for Pb–Pb collisions. The results are plotted versus the transverse momentum per nucleon. A clear decrease of B_2 and B_3 with increasing centrality is observed. In the coalescence picture, this behavior is explained by an increase in the source volume V_{eff}: the larger the distance between the protons and neutrons which are created in the collision, the less likely is that they coalesce. Alternatively, it can be understood on the basis of the approximately constant d/p and ^{3}He/p-ratios as an increase of the overall proton multiplicity independent of the geometry of the collision. The argument can be best illustrated by assuming a constant value of B_2 and integrating Eq. (8) over p_T. The value of B_2 can then be calculated for a given ratio d/p and a given spectral shape $f(p_T)$ (with $\int_0^\infty f(p_T) \, dp_T = 1$) of the proton spectrum as

$$B_2 = \frac{\pi}{2} \cdot \frac{\frac{dN_d}{dy}}{(\frac{dN_p}{dy})^2} \cdot \frac{1}{\int_0^\infty \frac{f^2(p_T)}{p_T} dp_T} , \tag{11}$$

where for a constant ratio of the deuteron dN_d/dy to proton dN_p/dy yield, it is found that $B_2 \propto 1/(dN_p/dy)$. As can be seen in Fig. 18, the coalescence parameter also develops an increasing trend with transverse momentum for central collisions in contrast to expectations of the most simple coalescence models. The significance of this increase is further substantiated by the fact that the systematic errors between p_T-bins are to a large extent correlated. It can be qualitatively explained by position-momentum correlations which are caused by a radially expanding source [58]. A comparison of the B_2 and B_3 values based on Eq. (10) is presented in Fig. 19 and shows qualitative agreement between the two observables.

In a more quantitative picture, it turns out that the coalescence process is governed by the same homogeneity volume which can be extracted from the HBT radii. The mathematical expression which relates B_2 to HBT radii ($R_\perp$ and $R_\parallel$) is given by

$$B_2 = \frac{3\pi^{3/2} \langle C_d \rangle}{2 m_T R_\perp^2 (m_T) R_\parallel (m_T)} , \tag{12}$$
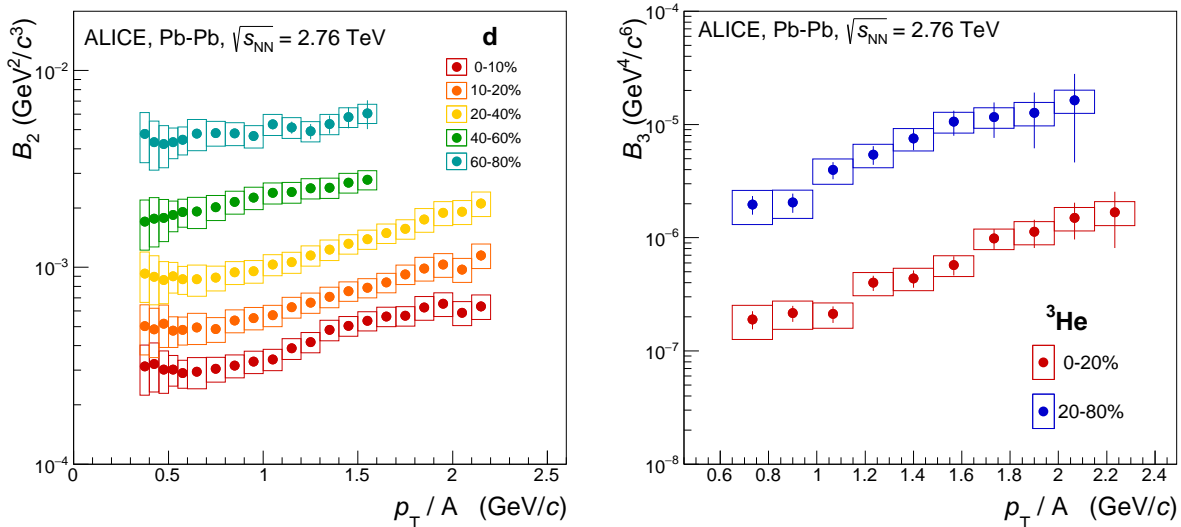
Fig. 18: The coalescence parameters B_2 (left) and B_3 (right) as a function of the transverse momentum per nucleon for various centrality classes in Pb–Pb collisions at $\sqrt{s_{NN}}$ = 2.76 TeV.

where m_T corresponds to the transverse mass [14]. $R_{\parallel}$ and $R_{\perp}$ are given by the longitudinal and transverse HBT radii in the Yano-Koonin-Podgoretskii parameterization. $\langle C_d \rangle$ is a quantum-mechanical correction factor which depends on the deuteron size and the longitudinal and transverse radii of homogeneity for nucleons. As explained in detail in [14], Eq. (12) is only valid for gaussian density profiles of the fireball. The latter would lead to identical slopes T_d^* and T_p^* of the deuteron and proton spectra which is not supported by data. For the phenomenologically more preferred box-like density profiles, the equation must be in principle amended by the factor $\exp\left(2(m_T - m_0)(\frac{1}{T_p^*} - \frac{1}{T_d^*})\right)$ where m_0 corresponds to the rest mass of the proton. For reasons of simplicity, this additional correction, which would lead to an even steeper increase of the B_2 values from HBT as a function of p_T, is neglected in the following. Figure 19 shows the comparison of B_2 values from Fig. 18 obtained in the 0-20% centrality interval with B_2 calculated using Eq. (12) and the HBT volume $V_{eff} = R_{\perp}^2 R_{\parallel} = R_{side}^2 R_{long}$ from [59, 60] for pions[†]. The dependence of the HBT radii on the particle mass is taken into account by showing results as a function of the transverse kinetic energy per nucleon. A rough agreement is found in terms of magnitude and the dependence on p_T.

Taking into account its strong dependence on centrality and p_T, the dependence of B_2 on collision energy can also be discussed. It is observed that B_2 at a fixed momentum ($p_T = 1.3$ GeV/c) for central collisions (0-20%) decreases rapidly from AGS energies to top SPS energy and then remains about the same up to RHIC [51]. Our value of approximately 4×10^{-4} GeV^2/c^3 is only slightly lower than the measurement at RHIC ($\approx 6 \times 10^{-4}$ GeV^2/c^3). Since B_2 is inversely proportional to the homogeneity volume $V_{eff} = R_{\perp}^2 R_{\parallel}$, the decrease in B_2 corresponds to an increase in effective volume and supports similar observations based on HBT measurements. On the other hand, Eq. (11) shows that a decrease in B_2 can also be related to a simple increase of the proton multiplicity.

5 Conclusion

In summary, the spectral distributions of deuterons in pp at $\sqrt{s} = 7$ TeV and of deuterons and ^{3}He in Pb–Pb collisions at $\sqrt{s_{NN}} = 2.76$ TeV have been presented. In Pb–Pb collisions, the yields are decreasing by a factor of 307 ± 76 for each additional nucleon, the mean p_T rises with mass and the combined blast-

---

[†]The identity $R_{\perp}^2 R_{\parallel} = R_{side}^2 R_{long}$ is only valid for symmetric collision systems like Pb–Pb and for radii calculated in the longitudinally co-moving system.
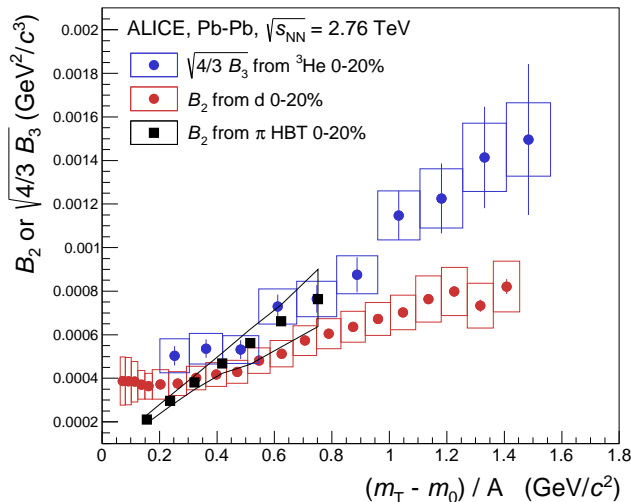
Fig. 19: The comparison of coalescence parameters B_2 and B_3 based on Eq. (10) as well as a comparison of B_2 values extracted from deuteron spectra and from HBT radii via Eq. (12) in central (0-20%) Pb–Pb collisions at $\sqrt{s_{NN}}$ = 2.76 TeV [59, 60].

wave fit to π, K, p, d, and ^{3}He gives a reasonable fit with $\langle\beta\rangle = 0.63$ and T_{kin} around 115 MeV suggesting that these nuclei take part in the evolution from chemical to kinetic freeze-out. For anti-tritons, a track-by-track identification has been applied in the momentum range 0.6 GeV/c < p_T < 1.6 GeV/c and the observation of 31 anti-tritons in Pb–Pb collisions at $\sqrt{s_{NN}}$ = 2.76 TeV in the 0-80% centrality class is reported in this paper.

An important question is whether the nuclei produced in heavy-ion collisions are created at the chemical freeze-out or at a later stage via coalescence. One of the key observations is the fact that the d/p and ^{3}He/p ratios are constant as a function of $\langle dN_{ch}/d\eta\rangle_{\eta=0}$. This confirms a trend seen by PHENIX [47, 51] for the d/p ratio. Such a behavior is expected from a thermal-statistical interpretation, as it is found that T_{chem} and μ_B do not vary with centrality in high energy collisions. A further test of the underlying production mechanism is the study of the elliptic flow (v_2) of these particles, presently under investigation. Results from the STAR Collaboration [8] indicate that v_2 scales with the number of nucleons when plotted versus p_T divided by the mass number. Such a behavior favors the coalescence model.

Studying the measured particle ratios from Pb–Pb collisions in a thermal-statistical model points to a common freeze-out temperature of around 156 MeV for light (anti-)nuclei and all other measured light flavor hadrons. At these temperatures, the weakly-bound deuteron and ^{3}He can hardly survive. These nuclei might break up and might be regenerated. However, if this complex process of break-up and regeneration is governed by an overall isentropic expansion, the particle ratios are preserved [61]. Eventually, the yields of particles including weakly bound nuclei are therefore described in the thermal-statistical model. Other properties, e.g. spectral shapes and elliptic flow, exhibit the influence of the interactions during the hadronic phase. Light (anti-)nuclei in Pb–Pb collisions therefore show the identical behavior as non-composite light flavor hadrons which are governed by a common chemical freeze-out and a subsequent hydrodynamic expansion.

The extracted coalescence parameters B_2 and B_3 exhibit a significant decrease with collision centrality and an increase with transverse momentum which cannot be explained by coalescence models in their simplest form. On the other hand, taking into account the larger source volume for more central collisions and the radial expansion of the emitting system, a rough agreement with the B_2 parameter deduced from the HBT radii of pions is found. Thus the production of light (anti-)nuclei in Pb–Pb collisions may still

be compatible with the expectations from a coalescence space-time description.

The measurements of nuclei at LHC energies are shown to follow trends observed from lower incident energies. Extrapolations and model predictions based on the thermal-statistical or coalescence approach are, therefore, a solid ground for further studies, e.g. of hyper-nuclei and exotica.

Acknowledgements

References

[1] A. Andronic, P. Braun-Munzinger, J. Stachel, and H. Stoecker, "Production of light nuclei, hypernuclei and their antiparticles in relativistic nuclear collisions," *Phys. Lett.* **B697** (2011) 203–207, arXiv:1010.2995 [nucl-th].

[2] J. Cleymans, S. Kabana, I. Kraus, H. Oeschler, K. Redlich, *et al.*, "Antimatter production in proton-proton and heavy-ion collisions at ultrarelativistic energies," *Phys. Rev.* **C84** (2011) 054916, arXiv:1105.3719 [hep-ph].

[3] A. Andronic, P. Braun-Munzinger, K. Redlich, and J. Stachel, "The thermal model on the verge of the ultimate test: particle production in Pb-Pb collisions at the LHC," *J. Phys.* **G38** (2011) 124081, arXiv:1106.6321 [nucl-th].

[4] S. Butler and C. Pearson, "Deuterons from high-energy proton bombardment of matter," *Phys. Rev.* **129** (1963) 836–842.

[5] J. I. Kapusta, "Mechanisms for deuteron production in relativistic nuclear collisions," *Phys. Rev.* **C21** (1980) 1301–1310.

[6] **NA49** Collaboration, S. Afanasev *et al.*, "Deuteron production in central Pb + Pb collisions at 158-A-GeV," *Phys. Lett.* **B486** (2000) 22–28.

[7] **STAR** Collaboration, C. Adler *et al.*, "Antideuteron and anti-helium-3 production in $\sqrt{s_{NN}}$ = 130-GeV Au + Au collisions," *Phys. Rev. Lett.* **87** (2001) 262301, arXiv:nucl-ex/0108022.

[8] **STAR** Collaboration, B. Abelev *et al.*, "Yields and elliptic flow of d(anti-d) and He-3(anti-He-3) in Au + Au collisions at $\sqrt{s_{NN}}$ = 200- GeV," arXiv:0909.0566 [nucl-ex].

[9] **ALEPH** Collaboration, S. Schael *et al.*, "Deuteron and anti-deuteron production in e+ e- collisions at the Z resonance," *Phys. Lett.* **B639** (2006) 192–201, arXiv:hep-ex/0604023 [hep-ex].

[10] **H1** Collaboration, A. Aktas *et al.*, "Measurement of anti-deuteron photoproduction and a search for heavy stable charged particles at HERA," *Eur. Phys. J.* **C36** (2004) 413–423, arXiv:hep-ex/0403056 [hep-ex].

[11] V. Abramov, B. Y. Baldin, A. Buzulutskov, V. Y. Glebov, A. Dyshkant, *et al.*, "High p_T Deuteron and Anti-deuteron Production in pp and pA Collisions at 70-GeV," *Sov. J. Nucl. Phys.* **45** (1987) 845.

[12] **NA49** Collaboration, T. Anticic *et al.*, "Energy and centrality dependence of deuteron and proton production in Pb + Pb collisions at relativistic energies," *Phys. Rev.* **C69** (2004) 024902.

[13] I. Bearden, H. Boggild, J. Boissevain, P. Christiansen, L. Conin, *et al.*, "Anti-deuteron production in 158-A-GeV/c Pb + Pb collisions," *Phys. Rev. Lett.* **85** (2000) 2681–2684.

[14] R. Scheibl and U. W. Heinz, "Coalescence and flow in ultrarelativistic heavy ion collisions," *Phys. Rev.* **C59** (1999) 1585–1602, arXiv:nucl-th/9809092 [nucl-th].

[15] J. Steinheimer, K. Gudima, A. Botvina, I. Mishustin, M. Bleicher, *et al.*, "Hypernuclei, dibaryon and antinuclei production in high energy heavy ion collisions: Thermal production versus Coalescence," *Phys. Lett.* **B714** (2012) 85–91, arXiv:1203.2547 [nucl-th].

[16] **NA52** Collaboration, R. Arsenescu *et al.*, "An Investigation of the anti-nuclei and nuclei production mechanism in Pb + Pb collisions at 158-A-GeV," *New J. Phys.* **5** (2003) 150.

[17] H. Gutbrod, A. Sandoval, P. Johansen, A. M. Poskanzer, J. Gosset, *et al.*, "Final state interactions in the production of hydrogen and helium isotopes by relativistic heavy ions on uranium," *Phys. Rev. Lett.* **37** (1976) 667–670.

[18] **E814** Collaboration, J. Barrette *et al.*, "Production of light nuclei in relativistic heavy ion collisions," *Phys. Rev.* **C50** (1994) 1077–1084.

[19] P. Braun-Munzinger and J. Stachel, "Production of strange clusters and strange matter in nucleus-nucleus collisions at the AGS," *J. Phys.* **G21** (1995) L17–L20, `arXiv:nucl-th/9412035 [nucl-th]`.

[20] **E864** Collaboration, T. Armstrong *et al.*, "Measurements of light nuclei production in 11.5-A-GeV/c Au + Pb heavy ion collisions," *Phys. Rev.* **C61** (2000) 064908, `arXiv:nucl-ex/0003009 [nucl-ex]`.

[21] **STAR** Collaboration, H. Agakishiev *et al.*, "Observation of the antimatter helium-4 nucleus," *Nature* **473** (2011) 353, `arXiv:1103.3312 [nucl-ex]`.

[22] **STAR** Collaboration, B. I. Abelev *et al.*, "Observation of an Antimatter Hypernucleus," *Science* **328** (2010) 58–62, `arXiv:1003.2030 [nucl-ex]`.

[23] **ALICE** Collaboration, K. Aamodt *et al.*, "The ALICE experiment at the CERN LHC," *JINST* **3** (2008) S08002.

[24] **ALICE** Collaboration, B. B. Abelev *et al.*, "Performance of the ALICE Experiment at the CERN LHC," *Int. J. Mod. Phys.* **A29** (2014) 1430044, `arXiv:1402.4476 [nucl-ex]`.

[25] J. Alme *et al.*, "The ALICE TPC, a large 3-dimensional tracking device with fast readout for ultra-high multiplicity events," *Nucl. Instrum. Meth.* **A622** (2010) 316–367, `arXiv:arXiv:1001.1950 [physics.ins-det]`.

[26] A. Akindinov, A. Alici, P. Antonioli, S. Arcelli, M. Basile, *et al.*, "Results of the ALICE time-of-flight detector from the 2009 cosmic-ray data taking," *Eur. Phys. J.* **C68** (2010) 601–607.

[27] **ALICE** Collaboration, K. Aamodt *et al.*, "Alignment of the ALICE Inner Tracking System with cosmic-ray tracks," *JINST* **5** (2010) P03003, `arXiv:1001.0502 [physics.ins-det]`.

[28] **ALICE** Collaboration, B. Abelev *et al.*, "Centrality determination of Pb-Pb collisions at $\sqrt{s_{NN}} =$ 2.76 TeV with ALICE," *Phys. Rev.* **C88** (2013) 044909, `arXiv:1301.4361 [nucl-ex]`.

[29] T. Sjostrand, S. Mrenna, and P. Z. Skands, "PYTHIA 6.4 Physics and Manual," *JHEP* **0605** (2006) 026, `arXiv:hep-ph/0603175 [hep-ph]`.

[30] R. Engel, J. Ranft, and S. Roesler, "Hard diffraction in hadron hadron interactions and in photoproduction," *Phys. Rev.* **D52** (1995) 1459–1468, `arXiv:hep-ph/9502319 [hep-ph]`.

[31] X.-N. Wang and M. Gyulassy, "HIJING: A Monte Carlo model for multiple jet production in pp, pA and AA collisions," *Phys. Rev.* **D44** (1991) 3501–3516.

[32] R. Brun, F. Carminati, and S. Giani, "GEANT Detector Description and Simulation Tool,".

[33] **GEANT4** Collaboration, S. Agostinelli *et al.*, "GEANT4: A Simulation toolkit," *Nucl. Instrum. Meth.* **A506** (2003) 250–303.

[34] V. Uzhinsky, J. Apostolakis, A. Galoyan, G. Folger, V. Grichine, *et al.*, "Antinucleus-nucleus cross sections implemented in Geant4," *Phys. Lett.* **B705** (2011) 235–239.

[35] **ALICE** Collaboration, E. Abbas *et al.*, "Mid-rapidity anti-baryon to baryon ratios in pp collisions at $\sqrt{s}$ = 0.9, 2.76 and 7 TeV measured by ALICE," *Eur. Phys. J.* **C73** (2013) 2496, `arXiv:1305.1562 [nucl-ex]`.

[36] **ALICE** Collaboration, B. B. Abelev *et al.*, "K_S^0 and Λ production in Pb-Pb collisions at $\sqrt{s_{NN}}$ = 2.76 TeV," *Phys. Rev. Lett.* **111** (2013) 222301, `arXiv:1307.5530 [nucl-ex]`.

[37] H. Kamada, J. Golak, K. Miyagawa, H. Witala, and W. Gloeckle, "Pi mesonic decay of the hypertriton," *Phys. Rev.* **C57** (1998) 1595–1603, `arXiv:nucl-th/9709035 [nucl-th]`.

[38] S. Denisov, S. Donskov, Y. Gorin, V. Kachanov, V. Kutjin, *et al.*, "Measurements of anti-deuteron absorption and stripping cross sections at the momentum 13.3 Gev/c," *Nucl. Phys.* **B31** (1971) 253–260.

[39] F. Binon, S. Denisov, S. Donskov, P. Duteil, G. Giacomelli, *et al.*, "Absorption cross-sections of 25 Gev/c antideuterons in Li, C, Al, Cu and Pb," *Phys. Lett.* **B31** (1970) 230–232.

[40] A. A. Moiseev and J. F. Ormes, "Inelastic cross section for antihelium on nuclei: an empirical formula for use in the experiments to search for cosmic antimatter," *Astropart. Phys.* **6** (April, 1997) 379–386.

[41] **ALICE** Collaboration, B. Abelev *et al.*, "Centrality dependence of π, K, p production in Pb-Pb collisions at $\sqrt{s_{NN}}$ = 2.76 TeV," *Phys. Rev.* **C88** (2013) 044910, `arXiv:1303.0737 [hep-ex]`.

[42] **ALICE** Collaboration, B. Abelev *et al.*, "Measurement of inelastic, single- and double-diffraction cross sections in proton–proton collisions at the LHC with ALICE," *Eur. Phys. J.* **C73** (2013) 2456, `arXiv:1208.4968 [hep-ex]`.

[43] **ALICE** Collaboration, B. B. Abelev *et al.*, "Energy Dependence of the Transverse Momentum Distributions of Charged Particles in pp Collisions Measured by ALICE," *Eur. Phys. J.* **C73** no. 12, (2013) 2662, `arXiv:1307.1093 [nucl-ex]`.

[44] C. Tsallis, "Possible Generalization of Boltzmann-Gibbs Statistics," *J. Statist. Phys.* **52** (1988) 479–487.

[45] **STAR** Collaboration, B. I. Abelev *et al.*, "Strange particle production in p + p collisions at $\sqrt{s}$ = 200-GeV," *Phys. Rev.* **C75** (2007) 064901, `arXiv:nucl-ex/0607033`.

[46] **ALICE** Collaboration, K. Aamodt *et al.*, "Transverse momentum spectra of charged particles in proton-proton collisions at $\sqrt{s}$ = 900 GeV with ALICE at the LHC," *Phys. Lett.* **B693** (2010) 53–68, `arXiv:1007.0719 [hep-ex]`.

[47] **PHENIX** Collaboration, S. Adler *et al.*, "Identified charged particle spectra and yields in Au+Au collisions at $\sqrt{s_{NN}}$ = 200-GeV," *Phys. Rev.* **C69** (2004) 034909, `arXiv:nucl-ex/0307022 [nucl-ex]`.

[48] E. Schnedermann, J. Sollfrank, and U. W. Heinz, "Thermal phenomenology of hadrons from 200-A/GeV S+S collisions," *Phys. Rev.* **C48** (1993) 2462–2475, `arXiv:9307020 [nucl-th]`.

[49] **ALICE** Collaboration, B. Abelev *et al.*, "Pion, Kaon, and Proton Production in Central Pb–Pb Collisions at $\sqrt{s_{NN}}$ = 2.76 TeV," *Phys. Rev. Lett.* **109** (2012) 252301, `arXiv:1208.1974 [hep-ex]`.

[50] **STAR** Collaboration, J. Adams *et al.*, "Experimental and theoretical challenges in the search for the quark gluon plasma: The STAR Collaboration's critical assessment of the evidence from RHIC collisions," *Nucl. Phys.* **A757** (2005) 102–183, `arXiv:0501009 [nucl-ex]`.

[51] **PHENIX** Collaboration, S. Adler *et al.*, "Deuteron and antideuteron production in Au + Au collisions at $\sqrt{s_{NN}}$ = 200-GeV," *Phys. Rev. Lett.* **94** (2005) 122302, `arXiv:nucl-ex/0406004 [nucl-ex]`.

[52] **STAR** Collaboration, B. Abelev *et al.*, "Systematic Measurements of Identified Particle Spectra in *pp*, d+Au and Au+Au Collisions from STAR," *Phys. Rev.* **C79** (2009) 034909, `arXiv:0808.2041 [nucl-ex]`.

[53] G. Chen, H. Chen, J. Wu, D.-S. Li, and M.-J. Wang, "Centrality dependence of light (anti)nuclei and (anti)hypertriton production in Au+Au collisions at $\sqrt{s_{NN}}$ = 200 GeV," *Phys. Rev. C* **88** (Sep, 2013) 034908. `http://link.aps.org/doi/10.1103/PhysRevC.88.034908`.

[54] S. Wheaton and J. Cleymans, "THERMUS: A Thermal model package for ROOT," *Comput. Phys. Commun.* **180** (2009) 84–106, `arXiv:0407174 [hep-ph]`.

[55] J. Stachel, A. Andronic, P. Braun-Munzinger, and K. Redlich, "Confronting LHC data with the statistical hadronization model," *J. Phys. Conf. Ser.* **509** (2014) 012019, `arXiv:1311.4662 [nucl-th]`.

[56] L. Csernai and J. I. Kapusta, "Entropy and Cluster Production in Nuclear Collisions," *Phys.Rept.* **131** (1986) 223–318.

[57] A. Schwarzschild and C. Zupancic, "Production of Tritons, Deuterons, Nucleons, and Mesons by 30-GeV Protons on A-1, Be, and Fe Targets," *Phys.Rev.* **129** (1963) 854–862.

[58] A. Polleri, J. P. Bondorf, and I. N. Mishustin, "Effects of collective expansion on light cluster spectra in relativistic heavy ion collisions," *Phys. Lett.* **B419** (1998) 19–24, `arXiv:nucl-th/9711011 [nucl-th]`.

[59] **ALICE** Collaboration, K. Aamodt *et al.*, "Two-pion Bose-Einstein correlations in central Pb-Pb collisions at $\sqrt{s_{NN}}$ = 2.76 TeV," *Phys. Lett.* **B696** (2011) 328–337, `arXiv:1012.4035 [nucl-ex]`.

[60] **ALICE** Collaboration, B. Abelev *et al.*, "Centrality dependence pion femtoscopy in Pb–Pb collisions at $\sqrt{s_{NN}}$ = 2.76 TeV," *in preparation* .

[61] P. J. Siemens and J. I. Kapusta, "Evidence for a soft nuclear matter equation of state," *Phys. Rev. Lett.* **43** (1979) 1486–1489.

A   The ALICE Collaboration

J. Adam[40] , D. Adamová[83] , M.M. Aggarwal[87] , G. Aglieri Rinella[36] , M. Agnello[111] , N. Agrawal[48] ,
Z. Ahammed[131] , I. Ahmed[16] , S.U. Ahn[68] , I. Aimo[94 ,111] , S. Aiola[135] , M. Ajaz[16] , A. Akindinov[58] ,
S.N. Alam[131] , D. Aleksandrov[100] , B. Alessandro[111] , D. Alexandre[102] , R. Alfaro Molina[64] , A. Alici[105 ,12] ,
A. Alkin[3] , J. Alme[38] , T. Alt[43] , S. Altinpinar[18] , I. Altsybeev[130] , C. Alves Garcia Prado[119] , C. Andrei[78] ,
A. Andronic[97] , V. Anguelov[93] , J. Anielski[54] , T. Antičić[98] , F. Antinori[108] , P. Antonioli[105] , L. Aphecetche[113] ,
H. Appelshäuser[53] , S. Arcelli[28] , N. Armesto[17] , R. Arnaldi[111] , T. Aronsson[135] , I.C. Arsene[22] , M. Arslandok[53] ,
A. Augustinus[36] , R. Averbeck[97] , M.D. Azmi[19] , M. Bach[43] , A. Badalà[107] , Y.W. Baek[44] , S. Bagnasco[111] ,
R. Bailhache[53] , R. Bala[90] , A. Baldisseri[15] , M. Ball[92] , F. Baltasar Dos Santos Pedrosa[36] , R.C. Baral[61] ,
A.M. Barbano[111] , R. Barbera[29] , F. Barile[33] , G.G. Barnaföldi[134] , L.S. Barnby[102] , V. Barret[70] , P. Bartalini[7] ,
J. Bartke[116] , E. Bartsch[53] , M. Basile[28] , N. Bastid[70] , S. Basu[131] , B. Bathen[54] , G. Batigne[113] , A. Batista
Camejo[70] , B. Batyunya[66] , P.C. Batzing[22] , I.G. Bearden[80] , H. Beck[53] , C. Bedda[111] , N.K. Behera[49 ,48] ,
I. Belikov[55] , F. Bellini[28] , H. Bello Martinez[2] , R. Bellwied[121] , R. Belmont[133] , E. Belmont-Moreno[64] ,
V. Belyaev[76] , G. Bencedi[134] , S. Beole[27] , I. Berceanu[78] , A. Bercuci[78] , Y. Berdnikov[85] , D. Berenyi[134] ,
R.A. Bertens[57] , D. Berzano[36 ,27] , L. Betev[36] , A. Bhasin[90] , I.R. Bhat[90] , A.K. Bhati[87] , B. Bhattacharjee[45] ,
J. Bhom[127] , L. Bianchi[27 ,121] , N. Bianchi[72] , C. Bianchin[133 ,57] , J. Bielčík[40] , J. Bielčíková[83] , A. Bilandzic[80] ,
S. Biswas[79] , S. Bjelogrlic[57] , F. Blanco[10] , D. Blau[100] , C. Blume[53] , F. Bock[74 ,93] , A. Bogdanov[76] ,
H. Bøggild[80] , L. Boldizsár[134] , M. Bombara[41] , J. Book[53] , H. Borel[15] , A. Borissov[96] , M. Borri[82] , F. Bossú[65] ,
M. Botje[81] , E. Botta[27] , S. Böttger[52] , P. Braun-Munzinger[97] , M. Bregant[119] , T. Breitner[52] , T.A. Broker[53] ,
T.A. Browning[95] , M. Broz[40] , E.J. Brucken[46] , E. Bruna[111] , G.E. Bruno[33] , D. Budnikov[99] , H. Buesching[53] ,
S. Bufalino[36 ,111] , P. Buncic[36] , O. Busch[93] , Z. Buthelezi[65] , J.T. Buxton[20] , D. Caffarri[36 ,30] , X. Cai[7] ,
H. Caines[135] , L. Calero Diaz[72] , A. Caliva[57] , E. Calvo Villar[103] , P. Camerini[26] , F. Carena[36] , W. Carena[36] ,
J. Castillo Castellanos[15] , A.J. Castro[124] , E.A.R. Casula[25] , C. Cavicchioli[36] , C. Ceballos Sanchez[9] , J. Cepila[40] ,
P. Cerello[111] , B. Chang[122] , S. Chapeland[36] , M. Chartier[123] , J.L. Charvet[15] , S. Chattopadhyay[131] ,
S. Chattopadhyay[101] , V. Chelnokov[3] , M. Cherney[86] , C. Cheshkov[129] , B. Cheynis[129] , V. Chibante Barroso[36] ,
D.D. Chinellato[120] , P. Chochula[36] , K. Choi[96] , M. Chojnacki[80] , S. Choudhury[131] , P. Christakoglou[81] ,
C.H. Christensen[80] , P. Christiansen[34] , T. Chujo[127] , S.U. Chung[96] , C. Cicalo[106] , L. Cifarelli[12 ,28] ,
F. Cindolo[105] , J. Cleymans[89] , F. Colamaria[33] , D. Colella[33] , A. Collu[25] , M. Colocci[28] , G. Conesa Balbastre[71] ,
Z. Conesa del Valle[51] , M.E. Connors[135] , J.G. Contreras[11 ,40] , T.M. Cormier[84] , Y. Corrales Morales[27] , I. Cortés
Maldonado[2] , P. Cortese[32] , M.R. Cosentino[119] , F. Costa[36] , P. Crochet[70] , R. Cruz Albino[11] , E. Cuautle[63] ,
L. Cunqueiro[36] , T. Dahms[92 ,37] , A. Dainese[108] , A. Danu[62] , D. Das[101] , I. Das[51 ,101] , S. Das[4] , A. Dash[120] ,
S. Dash[48] , S. De[119] , A. De Caro[31 ,12] , G. de Cataldo[104] , J. de Cuveland[43] , A. De Falco[25] , D. De Gruttola[12 ,31] ,
N. De Marco[111] , S. De Pasquale[31] , A. Deisting[97 ,93] , A. Deloff[77] , E. Dénes[134 ,i] , G. D'Erasmo[33] , D. Di Bari[33] ,
A. Di Mauro[36] , P. Di Nezza[72] , M.A. Diaz Corchero[10] , T. Dietel[89] , P. Dillenseger[53] , R. Divià[36] ,
Ø. Djuvsland[18] , A. Dobrin[57 ,81] , T. Dobrowolski[77 ,i] , D. Domenicis Gimenez[119] , B. Dönigus[53] , O. Dordic[22] ,
A.K. Dubey[131] , A. Dubla[57] , L. Ducroux[129] , P. Dupieux[70] , R.J. Ehlers[135] , D. Elia[104] , H. Engel[52] ,
B. Erazmus[113 ,36] , F. Erhardt[128] , D. Eschweiler[43] , B. Espagnon[51] , M. Estienne[113] , S. Esumi[127] , J. Eum[96] ,
D. Evans[102] , S. Evdokimov[112] , G. Eyyubova[40] , L. Fabbietti[37 ,92] , D. Fabris[108] , J. Faivre[71] , A. Fantoni[72] ,
M. Fasel[74] , L. Feldkamp[54] , D. Felea[62] , A. Feliciello[111] , G. Feofilov[130] , J. Ferencei[83] , A. Fernández Téllez[2] ,
E.G. Ferreiro[17] , A. Ferretti[27] , A. Festanti[30] , J. Figiel[116] , M.A.S. Figueredo[123] , S. Filchagin[99] , D. Finogeev[56] ,
F.M. Fionda[104] , E.M. Fiore[33] , M.G. Fleck[93] , M. Floris[36] , S. Foertsch[65] , P. Foka[97] , S. Fokin[100] ,
E. Fragiacomo[110] , A. Francescon[36 ,30] , U. Frankenfeld[97] , U. Fuchs[36] , C. Furget[71] , A. Furs[56] , M. Fusco
Girard[31] , J.J. Gaardhøje[80] , M. Gagliardi[27] , A.M. Gago[103] , M. Gallio[27] , D.R. Gangadharan[74] , P. Ganoti[88] ,
C. Gao[7] , C. Garabatos[97] , E. Garcia-Solis[13] , C. Gargiulo[36] , P. Gasik[37 ,92] , M. Germain[113] , A. Gheata[36] ,
M. Gheata[36 ,62] , P. Ghosh[131] , S.K. Ghosh[4] , P. Gianotti[72] , P. Giubellino[36] , P. Giubilato[30] ,
E. Gladysz-Dziadus[116] , P. Glässel[93] , D.M. Gómez Coral[64] , A. Gomez Ramirez[52] , P. González-Zamora[10] ,
S. Gorbunov[43] , L. Görlich[116] , S. Gotovac[115] , V. Grabski[64] , L.K. Graczykowski[132] , A. Grelli[57] , A. Grigoras[36] ,
C. Grigoras[36] , V. Grigoriev[76] , A. Grigoryan[1] , S. Grigoryan[66] , B. Grinyov[3] , N. Grion[110] ,
J.F. Grosse-Oetringhaus[36] , J.-Y. Grossiord[129] , R. Grosso[36] , F. Guber[56] , R. Guernane[71] , B. Guerzoni[28] ,
K. Gulbrandsen[80] , H. Gulkanyan[1] , T. Gunji[126] , A. Gupta[90] , R. Gupta[90] , R. Haake[54] , Ø. Haaland[18] ,
C. Hadjidakis[51] , M. Haiduc[62] , H. Hamagaki[126] , G. Hamar[134] , L.D. Hanratty[102] , A. Hansen[80] , J.W. Harris[135] ,
H. Hartmann[43] , A. Harton[13] , D. Hatzifotiadou[105] , S. Hayashi[126] , S.T. Heckel[53] , M. Heide[54] , H. Helstrup[38] ,
A. Herghelegiu[78] , G. Herrera Corral[11] , B.A. Hess[35] , K.F. Hetland[38] , T.E. Hilden[46] , H. Hillemanns[36] ,
B. Hippolyte[55] , P. Hristov[36] , M. Huang[18] , T.J. Humanic[20] , N. Hussain[45] , T. Hussain[19] , D. Hutter[43] ,
D.S. Hwang[21] , R. Ilkaev[99] , I. Ilkiv[77] , M. Inaba[127] , C. Ionita[36] , M. Ippolitov[76 ,100] , M. Irfan[19] , M. Ivanov[97] ,
V. Ivanov[85] , V. Izucheev[112] , P.M. Jacobs[74] , C. Jahnke[119] , H.J. Jang[68] , M.A. Janik[132] , P.H.S.Y. Jayarathna[121] ,

C. Jena[30], S. Jena[121], R.T. Jimenez Bustamante[63], P.G. Jones[102], H. Jung[44], A. Jusko[102], P. Kalinak[59], A. Kalweit[36], J. Kamin[53], J.H. Kang[136], V. Kaplin[76], S. Kar[131], A. Karasu Uysal[69], O. Karavichev[56], T. Karavicheva[56], E. Karpechev[56], U. Kebschull[52], R. Keidel[137], D.L.D. Keijdener[57], M. Keil[36], K.H. Khan[16], M. Mohisin Khan[19], P. Khan[101], S.A. Khan[131], A. Khanzadeev[85], Y. Kharlov[112], B. Kileng[38], B. Kim[136], D.W. Kim[44 ,68], D.J. Kim[122], H. Kim[136], J.S. Kim[44], M. Kim[44], M. Kim[136], S. Kim[21], T. Kim[136], S. Kirsch[43], I. Kisel[43], S. Kiselev[58], A. Kisiel[132], G. Kiss[134], J.L. Klay[6], C. Klein[53], J. Klein[93], C. Klein-Bösing[54], A. Kluge[36], M.L. Knichel[93], A.G. Knospe[117], T. Kobayashi[127], C. Kobdaj[114], M. Kofarago[36], M.K. Köhler[97], T. Kollegger[97 ,43], A. Kolojvari[130], V. Kondratiev[130], N. Kondratyeva[76], E. Kondratyuk[112], A. Konevskikh[56], M. Kour[90], C. Kouzinopoulos[36], O. Kovalenko[77], V. Kovalenko[130], M. Kowalski[36 ,116], S. Kox[71], G. Koyithatta Meethaleveedu[48], J. Kral[122], I. Králik[59], A. Kravčáková[41], M. Krelina[40], M. Kretz[43], M. Krivda[102 ,59], F. Krizek[83], E. Kryshen[36], M. Krzewicki[97 ,43], A.M. Kubera[20], V. Kučera[83], Y. Kucheriaev[100 ,i], T. Kugathasan[36], C. Kuhn[55], P.G. Kuijer[81], I. Kulakov[43], A. Kumar[90], J. Kumar[48], L. Kumar[79 ,87], P. Kurashvili[77], A. Kurepin[56], A.B. Kurepin[56], A. Kuryakin[99], S. Kushpil[83], M.J. Kweon[50], Y. Kwon[136], S.L. La Pointe[111], P. La Rocca[29], C. Lagana Fernandes[119], I. Lakomov[51 ,36], R. Langoy[42], C. Lara[52], A. Lardeux[15], A. Lattuca[27], E. Laudi[36], R. Lea[26], L. Leardini[93], G.R. Lee[102], S. Lee[136], I. Legrand[36], J. Lehnert[53], R.C. Lemmon[82], V. Lenti[104], E. Leogrande[57], I. León Monzón[118], M. Leoncino[27], P. Lévai[134], S. Li[7 ,70], X. Li[14], J. Lien[42], R. Lietava[102], S. Lindal[22], V. Lindenstruth[43], C. Lippmann[97], M.A. Lisa[20], H.M. Ljunggren[34], D.F. Lodato[57], P.I. Loenne[18], V.R. Loggins[133], V. Loginov[76], C. Loizides[74], X. Lopez[70], E. López Torres[9], A. Lowe[134], X.-G. Lu[93], P. Luettig[53], M. Lunardon[30], G. Luparello[26 ,57], A. Maevskaya[56], M. Mager[36], S. Mahajan[90], S.M. Mahmood[22], A. Maire[55], R.D. Majka[135], M. Malaev[85], I. Maldonado Cervantes[63], L. Malinina[ii,66], D. Mal'Kevich[58], P. Malzacher[97], A. Mamonov[99], L. Manceau[111], V. Manko[100], F. Manso[70], V. Manzari[104 ,36], M. Marchisone[27], J. Mareš[60], G.V. Margagliotti[26], A. Margotti[105], J. Margutti[57], A. Marín[97], C. Markert[117], M. Marquard[53], N.A. Martin[97], J. Martin Blanco[113], P. Martinengo[36], M.I. Martínez[2], G. Martínez García[113], M. Martinez Pedreira[36], Y. Martynov[3], A. Mas[119], S. Masciocchi[97], M. Masera[27], A. Masoni[106], L. Massacrier[113], A. Mastroserio[33], H. Masui[127], A. Matyja[116], C. Mayer[116], J. Mazer[124], M.A. Mazzoni[109], D. Mcdonald[121], F. Meddi[24], A. Menchaca-Rocha[64], E. Meninno[31], J. Mercado Pérez[93], M. Meres[39], Y. Miake[127], M.M. Mieskolainen[46], K. Mikhaylov[58 ,66], L. Milano[36], J. Milosevic[22], L.M. Minervini[104 ,23], A. Mischke[57], A.N. Mishra[49], D. Miśkowiec[97], J. Mitra[131], C.M. Mitu[62], N. Mohammadi[57], B. Mohanty[79 ,131], L. Molnar[55], L. Montaño Zetina[11], E. Montes[10], M. Morando[30], D.A. Moreira De Godoy[113], L.A.P. Moreno[2], S. Moretto[30], A. Morreale[113], A. Morsch[36], V. Muccifora[72], E. Mudnic[115], D. Mühlheim[54], S. Muhuri[131], M. Mukherjee[131], H. Müller[36], J.D. Mulligan[135], M.G. Munhoz[119], S. Murray[65], L. Musa[36], J. Musinsky[59], B.K. Nandi[48], R. Nania[105], E. Nappi[104], M.U. Naru[16], C. Nattrass[124], K. Nayak[79], T.K. Nayak[131], S. Nazarenko[99], A. Nedosekin[58], L. Nellen[63], F. Ng[121], M. Nicassio[97], M. Niculescu[62 ,36], J. Niedziela[36], B.S. Nielsen[80], S. Nikolaev[100], S. Nikulin[100], V. Nikulin[85], F. Noferini[12 ,105], P. Nomokonov[66], G. Nooren[57], J. Norman[123], A. Nyanin[100], J. Nystrand[18], H. Oeschler[93], S. Oh[135], S.K. Oh[67], A. Ohlson[36], A. Okatan[69], T. Okubo[47], L. Olah[134], J. Oleniacz[132], A.C. Oliveira Da Silva[119], M.H. Oliver[135], J. Onderwaater[97], C. Oppedisano[111], A. Ortiz Velasquez[63], A. Oskarsson[34], J. Otwinowski[97 ,116], K. Oyama[93], M. Ozdemir[53], Y. Pachmayer[93], P. Pagano[31], G. Paić[63], C. Pajares[17], S.K. Pal[131], J. Pan[133], A.K. Pandey[48], D. Pant[48], V. Papikyan[1], G.S. Pappalardo[107], P. Pareek[49], W.J. Park[97], S. Parmar[87], A. Passfeld[54], V. Paticchio[104], B. Paul[101], T. Pawlak[132], T. Peitzmann[57], H. Pereira Da Costa[15], E. Pereira De Oliveira Filho[119], D. Peresunko[76 ,100], C.E. Pérez Lara[81], V. Peskov[53], Y. Pestov[5], V. Petráček[40], V. Petrov[112], M. Petrovici[78], C. Petta[29], S. Piano[110], M. Pikna[39], P. Pillot[113], O. Pinazza[105 ,36], L. Pinsky[121], D.B. Piyarathna[121], M. Płoskoń[74], M. Planinic[128], J. Pluta[132], S. Pochybova[134], P.L.M. Podesta-Lerma[118], M.G. Poghosyan[86], B. Polichtchouk[112], N. Poljak[128], W. Poonsawat[114], A. Pop[78], S. Porteboeuf-Houssais[70], J. Porter[74], J. Pospisil[83], S.K. Prasad[4], R. Preghenella[105 ,36], F. Prino[111], C.A. Pruneau[133], I. Pshenichnov[56], M. Puccio[111], G. Puddu[25], P. Pujahari[133], V. Punin[99], J. Putschke[133], H. Qvigstad[22], A. Rachevski[110], S. Raha[4], S. Rajput[90], J. Rak[122], A. Rakotozafindrabe[15], L. Ramello[32], R. Raniwala[91], S. Raniwala[91], S.S. Räsänen[46], B.T. Rascanu[53], D. Rathee[87], K.F. Read[124], J.S. Real[71], K. Redlich[77], R.J. Reed[133], A. Rehman[18], P. Reichelt[53], M. Reicher[57], F. Reidt[93 ,36], X. Ren[7], R. Renfordt[53], A.R. Reolon[72], A. Reshetin[56], F. Rettig[43], J.-P. Revol[12], K. Reygers[93], V. Riabov[85], R.A. Ricci[73], T. Richert[34], M. Richter[22], P. Riedler[36], W. Riegler[36], F. Riggi[29], C. Ristea[62], A. Rivetti[111], E. Rocco[57], M. Rodríguez Cahuantzi[11 ,2], A. Rodriguez Manso[81], K. Røed[22], E. Rogochaya[66], D. Rohr[43], D. Röhrich[18], R. Romita[123], F. Ronchetti[72], L. Ronflette[113], P. Rosnet[70], A. Rossi[36], F. Roukoutakis[88], A. Roy[49], C. Roy[55], P. Roy[101], A.J. Rubio Montero[10], R. Rui[26], R. Russo[27], E. Ryabinkin[100], Y. Ryabov[85], A. Rybicki[116], S. Sadovsky[112], K. Šafařík[36], B. Sahlmuller[53], P. Sahoo[49], R. Sahoo[49], S. Sahoo[61], P.K. Sahu[61], J. Saini[131], S. Sakai[72], M.A. Saleh[133], C.A. Salgado[17], J. Salzwedel[20], S. Sambyal[90], V. Samsonov[85], X. Sanchez Castro[55],

L. Šándor[59], A. Sandoval[64], M. Sano[127], G. Santagati[29], D. Sarkar[131], E. Scapparone[105], F. Scarlassara[30], R.P. Scharenberg[95], C. Schiaua[78], R. Schicker[93], C. Schmidt[97], H.R. Schmidt[35], S. Schuchmann[53], J. Schukraft[36], M. Schulc[40], T. Schuster[135], Y. Schutz[113,36], K. Schwarz[97], K. Schweda[97], G. Scioli[28], E. Scomparin[111], R. Scott[124], K.S. Seeder[119], J.E. Seger[86], Y. Sekiguchi[126], I. Selyuzhenkov[97], K. Senosi[65], J. Seo[67,96], E. Serradilla[10,64], A. Sevcenco[62], A. Shabanov[56], A. Shabetai[113], O. Shadura[3], R. Shahoyan[36], A. Shangaraev[112], A. Sharma[90], M. Sharma[90], N. Sharma[124,61], K. Shigaki[47], K. Shtejer[9,27], Y. Sibiriak[100], S. Siddhanta[106], K.M. Sielewicz[36], T. Siemiarczuk[77], D. Silvermyr[84,34], C. Silvestre[71], G. Simatovic[128], G. Simonetti[36], R. Singaraju[131], R. Singh[79], S. Singha[79,131], V. Singhal[131], B.C. Sinha[131], T. Sinha[101], B. Sitar[39], M. Sitta[32], T.B. Skaali[22], M. Slupecki[122], N. Smirnov[135], R.J.M. Snellings[57], T.W. Snellman[122], C. Søgaard[34], R. Soltz[75], J. Song[96], M. Song[136], Z. Song[7], F. Soramel[30], S. Sorensen[124], M. Spacek[40], E. Spiriti[72], I. Sputowska[116], M. Spyropoulou-Stassinaki[88], B.K. Srivastava[95], J. Stachel[93], I. Stan[62], G. Stefanek[77], M. Steinpreis[20], E. Stenlund[34], G. Steyn[65], J.H. Stiller[93], D. Stocco[113], P. Strmen[39], A.A.P. Suaide[119], T. Sugitate[47], C. Suire[51], M. Suleymanov[16], R. Sultanov[58], M. Šumbera[83], T.J.M. Symons[74], A. Szabo[39], A. Szanto de Toledo[119,i], I. Szarka[39], A. Szczepankiewicz[36], M. Szymanski[132], J. Takahashi[120], N. Tanaka[127], M.A. Tangaro[33], J.D. Tapia Takaki[iii,51], A. Tarantola Peloni[53], M. Tariq[19], M.G. Tarzila[78], A. Tauro[36], G. Tejeda Muñoz[2], A. Telesca[36], K. Terasaki[126], C. Terrevoli[30,25], B. Teyssier[129], J. Thäder[97,74], D. Thomas[117], R. Tieulent[129], A.R. Timmins[121], A. Toia[53], S. Trogolo[111], V. Trubnikov[3], W.H. Trzaska[122], T. Tsuji[126], A. Tumkin[99], R. Turrisi[108], T.S. Tveter[22], K. Ullaland[18], A. Uras[129], G.L. Usai[25], A. Utrobicic[128], M. Vajzer[83], M. Vala[59], L. Valencia Palomo[70], S. Vallero[27], J. Van Der Maarel[57], J.W. Van Hoorne[36], M. van Leeuwen[57], T. Vanat[83], P. Vande Vyvre[36], D. Varga[134], A. Vargas[2], M. Vargyas[122], R. Varma[48], M. Vasileiou[88], A. Vasiliev[100], A. Vauthier[71], V. Vechernin[130], A.M. Veen[57], M. Veldhoen[57], A. Velure[18], M. Venaruzzo[73], E. Vercellin[27], S. Vergara Limón[2], R. Vernet[8], M. Verweij[133], L. Vickovic[115], G. Viesti[30,i], J. Viinikainen[122], Z. Vilakazi[125], O. Villalobos Baillie[102], A. Villatoro Tello[2], A. Vinogradov[100], L. Vinogradov[130], Y. Vinogradov[99,i], T. Virgili[31], V. Vislavicius[34], Y.P. Viyogi[131], A. Vodopyanov[66], M.A. Völkl[93], K. Voloshin[58], S.A. Voloshin[133], G. Volpe[134,36], B. von Haller[36], I. Vorobyev[37,92], D. Vranic[36,97], J. Vrláková[41], B. Vulpescu[70], A. Vyushin[99], B. Wagner[18], J. Wagner[97], H. Wang[57], M. Wang[7,113], Y. Wang[93], D. Watanabe[127], M. Weber[36,121], S.G. Weber[97], J.P. Wessels[54], U. Westerhoff[54], J. Wiechula[35], J. Wikne[22], M. Wilde[54], G. Wilk[77], J. Wilkinson[93], M.C.S. Williams[105], B. Windelband[93], M. Winn[93], C.G. Yaldo[133], Y. Yamaguchi[126], H. Yang[57], P. Yang[7], S. Yano[47], S. Yasnopolskiy[100], Z. Yin[7], H. Yokoyama[127], I.-K. Yoo[96], V. Yurchenko[3], I. Yushmanov[100], A. Zaborowska[132], V. Zaccolo[80], A. Zaman[16], C. Zampolli[105], H.J.C. Zanoli[119], S. Zaporozhets[66], A. Zarochentsev[130], P. Závada[60], N. Zaviyalov[99], H. Zbroszczyk[132], I.S. Zgura[62], M. Zhalov[85], H. Zhang[18,7], X. Zhang[74], Y. Zhang[7], C. Zhao[22], N. Zhigareva[58], D. Zhou[7], Y. Zhou[80,57], Z. Zhou[18], H. Zhu[18,7], J. Zhu[113,7], X. Zhu[7], A. Zichichi[12,28], A. Zimmermann[93], M.B. Zimmermann[54,36], G. Zinovjev[3], M. Zyzak[43]

Affiliation notes

[i] Deceased

[ii] Also at: M.V. Lomonosov Moscow State University, D.V. Skobeltsyn Institute of Nuclear, Physics, Moscow, Russia

[iii] Also at: University of Kansas, Lawrence, Kansas, United States

Collaboration Institutes

[1] A.I. Alikhanyan National Science Laboratory (Yerevan Physics Institute) Foundation, Yerevan, Armenia

[2] Benemérita Universidad Autónoma de Puebla, Puebla, Mexico

[3] Bogolyubov Institute for Theoretical Physics, Kiev, Ukraine

[4] Bose Institute, Department of Physics and Centre for Astroparticle Physics and Space Science (CAPSS), Kolkata, India

[5] Budker Institute for Nuclear Physics, Novosibirsk, Russia

[6] California Polytechnic State University, San Luis Obispo, California, United States

[7] Central China Normal University, Wuhan, China

[8] Centre de Calcul de l'IN2P3, Villeurbanne, France

[9] Centro de Aplicaciones Tecnológicas y Desarrollo Nuclear (CEADEN), Havana, Cuba

[10] Centro de Investigaciones Energéticas Medioambientales y Tecnológicas (CIEMAT), Madrid, Spain

[11] Centro de Investigación y de Estudios Avanzados (CINVESTAV), Mexico City and Mérida, Mexico

[12] Centro Fermi - Museo Storico della Fisica e Centro Studi e Ricerche "Enrico Fermi", Rome, Italy

[13] Chicago State University, Chicago, Illinois, USA
[14] China Institute of Atomic Energy, Beijing, China
[15] Commissariat à l'Energie Atomique, IRFU, Saclay, France
[16] COMSATS Institute of Information Technology (CIIT), Islamabad, Pakistan
[17] Departamento de Física de Partículas and IGFAE, Universidad de Santiago de Compostela, Santiago de Compostela, Spain
[18] Department of Physics and Technology, University of Bergen, Bergen, Norway
[19] Department of Physics, Aligarh Muslim University, Aligarh, India
[20] Department of Physics, Ohio State University, Columbus, Ohio, United States
[21] Department of Physics, Sejong University, Seoul, South Korea
[22] Department of Physics, University of Oslo, Oslo, Norway
[23] Dipartimento di Elettrotecnica ed Elettronica del Politecnico, Bari, Italy
[24] Dipartimento di Fisica dell'Università 'La Sapienza' and Sezione INFN Rome, Italy
[25] Dipartimento di Fisica dell'Università and Sezione INFN, Cagliari, Italy
[26] Dipartimento di Fisica dell'Università and Sezione INFN, Trieste, Italy
[27] Dipartimento di Fisica dell'Università and Sezione INFN, Turin, Italy
[28] Dipartimento di Fisica e Astronomia dell'Università and Sezione INFN, Bologna, Italy
[29] Dipartimento di Fisica e Astronomia dell'Università and Sezione INFN, Catania, Italy
[30] Dipartimento di Fisica e Astronomia dell'Università and Sezione INFN, Padova, Italy
[31] Dipartimento di Fisica 'E.R. Caianiello' dell'Università and Gruppo Collegato INFN, Salerno, Italy
[32] Dipartimento di Scienze e Innovazione Tecnologica dell'Università del Piemonte Orientale and Gruppo Collegato INFN, Alessandria, Italy
[33] Dipartimento Interateneo di Fisica 'M. Merlin' and Sezione INFN, Bari, Italy
[34] Division of Experimental High Energy Physics, University of Lund, Lund, Sweden
[35] Eberhard Karls Universität Tübingen, Tübingen, Germany
[36] European Organization for Nuclear Research (CERN), Geneva, Switzerland
[37] Excellence Cluster Universe, Technische Universität München, Munich, Germany
[38] Faculty of Engineering, Bergen University College, Bergen, Norway
[39] Faculty of Mathematics, Physics and Informatics, Comenius University, Bratislava, Slovakia
[40] Faculty of Nuclear Sciences and Physical Engineering, Czech Technical University in Prague, Prague, Czech Republic
[41] Faculty of Science, P.J. Šafárik University, Košice, Slovakia
[42] Faculty of Technology, Buskerud and Vestfold University College, Vestfold, Norway
[43] Frankfurt Institute for Advanced Studies, Johann Wolfgang Goethe-Universität Frankfurt, Frankfurt, Germany
[44] Gangneung-Wonju National University, Gangneung, South Korea
[45] Gauhati University, Department of Physics, Guwahati, India
[46] Helsinki Institute of Physics (HIP), Helsinki, Finland
[47] Hiroshima University, Hiroshima, Japan
[48] Indian Institute of Technology Bombay (IIT), Mumbai, India
[49] Indian Institute of Technology Indore, Indore (IITI), India
[50] Inha University, Incheon, South Korea
[51] Institut de Physique Nucléaire d'Orsay (IPNO), Université Paris-Sud, CNRS-IN2P3, Orsay, France
[52] Institut für Informatik, Johann Wolfgang Goethe-Universität Frankfurt, Frankfurt, Germany
[53] Institut für Kernphysik, Johann Wolfgang Goethe-Universität Frankfurt, Frankfurt, Germany
[54] Institut für Kernphysik, Westfälische Wilhelms-Universität Münster, Münster, Germany
[55] Institut Pluridisciplinaire Hubert Curien (IPHC), Université de Strasbourg, CNRS-IN2P3, Strasbourg, France
[56] Institute for Nuclear Research, Academy of Sciences, Moscow, Russia
[57] Institute for Subatomic Physics of Utrecht University, Utrecht, Netherlands
[58] Institute for Theoretical and Experimental Physics, Moscow, Russia
[59] Institute of Experimental Physics, Slovak Academy of Sciences, Košice, Slovakia
[60] Institute of Physics, Academy of Sciences of the Czech Republic, Prague, Czech Republic
[61] Institute of Physics, Bhubaneswar, India
[62] Institute of Space Science (ISS), Bucharest, Romania
[63] Instituto de Ciencias Nucleares, Universidad Nacional Autónoma de México, Mexico City, Mexico

[64] Instituto de Física, Universidad Nacional Autónoma de México, Mexico City, Mexico
[65] iThemba LABS, National Research Foundation, Somerset West, South Africa
[66] Joint Institute for Nuclear Research (JINR), Dubna, Russia
[67] Konkuk University, Seoul, South Korea
[68] Korea Institute of Science and Technology Information, Daejeon, South Korea
[69] KTO Karatay University, Konya, Turkey
[70] Laboratoire de Physique Corpusculaire (LPC), Clermont Université, Université Blaise Pascal, CNRS–IN2P3, Clermont-Ferrand, France
[71] Laboratoire de Physique Subatomique et de Cosmologie, Université Grenoble-Alpes, CNRS-IN2P3, Grenoble, France
[72] Laboratori Nazionali di Frascati, INFN, Frascati, Italy
[73] Laboratori Nazionali di Legnaro, INFN, Legnaro, Italy
[74] Lawrence Berkeley National Laboratory, Berkeley, California, United States
[75] Lawrence Livermore National Laboratory, Livermore, California, United States
[76] Moscow Engineering Physics Institute, Moscow, Russia
[77] National Centre for Nuclear Studies, Warsaw, Poland
[78] National Institute for Physics and Nuclear Engineering, Bucharest, Romania
[79] National Institute of Science Education and Research, Bhubaneswar, India
[80] Niels Bohr Institute, University of Copenhagen, Copenhagen, Denmark
[81] Nikhef, Nationaal instituut voor subatomaire fysica, Amsterdam, Netherlands
[82] Nuclear Physics Group, STFC Daresbury Laboratory, Daresbury, United Kingdom
[83] Nuclear Physics Institute, Academy of Sciences of the Czech Republic, Řež u Prahy, Czech Republic
[84] Oak Ridge National Laboratory, Oak Ridge, Tennessee, United States
[85] Petersburg Nuclear Physics Institute, Gatchina, Russia
[86] Physics Department, Creighton University, Omaha, Nebraska, United States
[87] Physics Department, Panjab University, Chandigarh, India
[88] Physics Department, University of Athens, Athens, Greece
[89] Physics Department, University of Cape Town, Cape Town, South Africa
[90] Physics Department, University of Jammu, Jammu, India
[91] Physics Department, University of Rajasthan, Jaipur, India
[92] Physik Department, Technische Universität München, Munich, Germany
[93] Physikalisches Institut, Ruprecht-Karls-Universität Heidelberg, Heidelberg, Germany
[94] Politecnico di Torino, Turin, Italy
[95] Purdue University, West Lafayette, Indiana, United States
[96] Pusan National University, Pusan, South Korea
[97] Research Division and ExtreMe Matter Institute EMMI, GSI Helmholtzzentrum für Schwerionenforschung, Darmstadt, Germany
[98] Rudjer Bošković Institute, Zagreb, Croatia
[99] Russian Federal Nuclear Center (VNIIEF), Sarov, Russia
[100] Russian Research Centre Kurchatov Institute, Moscow, Russia
[101] Saha Institute of Nuclear Physics, Kolkata, India
[102] School of Physics and Astronomy, University of Birmingham, Birmingham, United Kingdom
[103] Sección Física, Departamento de Ciencias, Pontificia Universidad Católica del Perú, Lima, Peru
[104] Sezione INFN, Bari, Italy
[105] Sezione INFN, Bologna, Italy
[106] Sezione INFN, Cagliari, Italy
[107] Sezione INFN, Catania, Italy
[108] Sezione INFN, Padova, Italy
[109] Sezione INFN, Rome, Italy
[110] Sezione INFN, Trieste, Italy
[111] Sezione INFN, Turin, Italy
[112] SSC IHEP of NRC Kurchatov institute, Protvino, Russia
[113] SUBATECH, Ecole des Mines de Nantes, Université de Nantes, CNRS-IN2P3, Nantes, France
[114] Suranaree University of Technology, Nakhon Ratchasima, Thailand
[115] Technical University of Split FESB, Split, Croatia
[116] The Henryk Niewodniczanski Institute of Nuclear Physics, Polish Academy of Sciences, Cracow, Poland

[117] The University of Texas at Austin, Physics Department, Austin, Texas, USA
[118] Universidad Autónoma de Sinaloa, Culiacán, Mexico
[119] Universidade de São Paulo (USP), São Paulo, Brazil
[120] Universidade Estadual de Campinas (UNICAMP), Campinas, Brazil
[121] University of Houston, Houston, Texas, United States
[122] University of Jyväskylä, Jyväskylä, Finland
[123] University of Liverpool, Liverpool, United Kingdom
[124] University of Tennessee, Knoxville, Tennessee, United States
[125] University of the Witwatersrand, Johannesburg, South Africa
[126] University of Tokyo, Tokyo, Japan
[127] University of Tsukuba, Tsukuba, Japan
[128] University of Zagreb, Zagreb, Croatia
[129] Université de Lyon, Université Lyon 1, CNRS/IN2P3, IPN-Lyon, Villeurbanne, France
[130] V. Fock Institute for Physics, St. Petersburg State University, St. Petersburg, Russia
[131] Variable Energy Cyclotron Centre, Kolkata, India
[132] Warsaw University of Technology, Warsaw, Poland
[133] Wayne State University, Detroit, Michigan, United States
[134] Wigner Research Centre for Physics, Hungarian Academy of Sciences, Budapest, Hungary
[135] Yale University, New Haven, Connecticut, United States
[136] Yonsei University, Seoul, South Korea
[137] Zentrum für Technologietransfer und Telekommunikation (ZTT), Fachhochschule Worms, Worms, Germany